

www.acsami.org Research Article

Chemically Induced Magnetic Dead Shells in Superparamagnetic Ni Nanoparticles Deduced from Polarized Small-Angle Neutron Scattering

Bhaskar Das, Joseph T. Batley, Kathryn L. Krycka, Julie A. Borchers, Patrick Quarterman, Caroline Korostynski, My Nguyen, Ishita Kamboj, Eray S. Aydil, and Chris Leighton*



Cite This: ACS Appl. Mater. Interfaces 2022, 14, 33491-33504



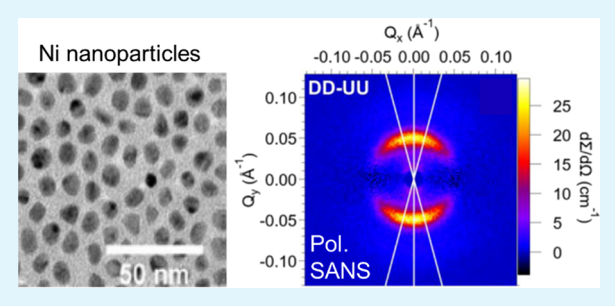
ACCESS I

III Metrics & More

Article Recommendations

Supporting Information

ABSTRACT: Advances in the synthesis and characterization of colloidal magnetic nanoparticles (NPs) have yielded great gains in the understanding of their complex magnetic behavior, with implications for numerous applications. Recent work using Ni NPs as a model soft ferromagnetic system, for example, achieved quantitative understanding of the superparamagnetic blocking temperature—particle diameter relationship. This hinged, however, on the critical assumption of a ferromagnetic NP volume lower than the chemical volume due to a nonferromagnetic dead shell indirectly deduced from magnetometry. Here, we determine both the chemical and magnetic average internal structures



of Ni NP ensembles *via* unpolarized, half-polarized, and fully polarized small-angle neutron scattering (SANS) measurements and analyses coupled with X-ray diffraction and magnetometry. The postulated nanometric magnetic dead shell is not only detected but conclusively identified as a non-ferromagnetic Ni phosphide derived from the trioctylphosphine commonly used in hot-injection colloidal NP syntheses. The phosphide shell thickness is tunable *via* synthesis temperature, falling to as little as 0.5 nm at 170 °C. Temperature- and magnetic field-dependent polarized SANS measurements additionally reveal essentially bulk-like ferromagnetism in the Ni core and negligible interparticle magnetic interactions, quantitatively supporting prior modeling of superparamagnetism. These findings advance the understanding of synthesis—structure—property relationships in metallic magnetic NPs, point to a simple potential route to ligand-free stabilization, and highlight the power of the currently available suite of polarized SANS measurement and analysis capabilities for magnetic NP science and technology.

KEYWORDS: magnetic nanoparticles, dead shell effects, colloidal synthesis, small-angle neutron scattering, polarized neutron scattering

■ INTRODUCTION

Chemical synthesis of colloidal magnetic nanoparticles (NPs) has advanced to the stage where NP size, dispersity, structure, ligand chemistry, and functionalization can be precisely controlled, enabling detailed, quantitative studies of their rich magnetic behavior. 1-6 The latter encompasses single-domain to multi-domain crossovers, superparamagnetic (SP) behavior, complex spin textures such as canted states, magnetic dead shells, surface effects such as enhanced magnetic anisotropy, and heterostructure effects in core/shell systems.7-19 These phenomena have drawn substantial interest from magnetism and magnetic materials communities, exploring both fundamental magnetism and synthesis-structure-property relationships.^{7–18} Simultaneously, important biomedical applications of magnetic NPs have emerged or are under development, including magnetic-NP-based hyperthermia cancer treatment, contrast enhancement in biomedical imaging, warming of cryopreserved tissue, $\it etc.^{20-24}$ The potential applicability of magnetic NPs to other technologies, such as magnetic recording, has also been discussed. $^{6,16-19,23,25-27}$

Regarding materials systems in magnetic NPs, the above biomedical applications have driven much interest in ferrimagnetic Fe₃O₄ and related oxides, ^{4,12,14,16,20–24,28} which has gradually expanded into complex oxides of interest for basic research. ^{29–37} On the other hand, potential magnetic recording applications, for example, have driven interest in hard (*i.e.*, high magnetocrystalline anisotropy) ferromagnetic (FM) systems, often metals and alloys such as Co, Co-Pt, Fe-Pt, *etc.* ^{25,27,38–42} Due to this particular emphasis on oxides and hard FM metals and alloys, soft (*i.e.*, low magnetocrystalline anisotropy) FM metals and alloys (*e.g.*, Ni, Ni-Fe) have been relatively underexplored in NP form. This is despite their relevance in applications such as electromagnetic interference

Received: March 29, 2022 Accepted: July 5, 2022 Published: July 17, 2022





shielding and wireless charging/heating technologies.⁴³ Our recent prior work thus focused on elemental Ni NPs as a model soft FM system, in particular using thoroughly characterized NP ensembles to demonstrate quantitative understanding of the SP behavior that dominates their magnetism.⁴⁴

Briefly, superparamagnetism in FM NPs arises due to competition between magnetic anisotropy (which acts to lock the magnetization vector in specific orientations) with thermally induced fluctuations of the magnetization vector. In the Néel–Brown–Arrhenius picture, as temperature (T) increases, the characteristic timescale of the fluctuations (τ) decreases exponentially, controlled by $K_{\rm eff}V/k_{\rm B}T$, where $K_{\rm eff}$ is the effective magnetic anisotropy constant, V is the NP volume, and $k_{\rm B}$ is Boltzmann's constant. On a specific measurement time scale $\tau_{\rm m}$, above some T, referred to as the SP blocking temperature ($T_{\rm B}$), the magnetization vector thus begins to fluctuate within the measurement window, time averaging the magnetization to zero (in zero applied magnetic field, H). 16,46,47,51 In the simplest model, $T_{\rm B}$ is given by

$$T_{\rm B} = \frac{K_{\rm eff}V}{k_{\rm B}\ln\left(\frac{\tau_{\rm m}}{\tau_{\rm o}}\right)} \tag{1}$$

where τ_0 is an inverse attempt frequency of $\sim 10^{-10}$ to 10^{-9} s. $^{46-48}$ At $T < T_B$, the system is referred to as "blocked" and is essentially FM, whereas at $T > T_B$, the system is referred to as "unblocked" or SP. In principle, super-paramagnetism is thus a relatively simple phenomenon, accessible to quantitative understanding. 52-57 In practice, however, real FM NP ensembles possess myriad complicating factors. 57-60 These include the inevitable distributions around the average diameter $\langle D \rangle$ (which trivially result in distributions in V and $T_{\rm B}$), the subsequent challenge of accurately determining the average blocking temperature $\langle T_{\rm B} \rangle$, the substantial complexity in $K_{\rm eff}$ (which can include defect and surface contributions in addition to the magnetocrystalline anisotropy of the ferromagnet), possible interparticle interactions, surface dead shell effects that reduce the effective magnetic volume below the chemical volume V, and many others. 57-63

Given the above, our recent demonstration of quantitative, parameter-free agreement with eq 1 is significant. 44 This was achieved in thoroughly characterized Ni NP ensembles synthesized via hot injection of a Ni acetate-oleylamine (OAm) complex into trioctylphosphine (TOP), using the TOP/OAm ratio, synthesis temperature (T_s) , reaction time, and post-synthesis centrifugation conditions as control parameters. This resulted in Ni NP ensembles with 4.7 nm \leq <D> \leq 22.3 nm, and average relative dispersity σ /<D> = 0.2, reaching ~0.1 under the best conditions. 44 The NPs were found to be composed of face-centered-cubic (FCC) Ni with bulk-like lattice parameters and twinned and/or polycrystalline character, 44 with both OAm and TOP serving as ligands on the NP surfaces.⁴⁴ Most significantly, extensive measurement and careful analysis of the T-dependent magnetization (M) after field-cooling (FC) and zero-field-cooling (ZFC) were used to determine not only $\langle T_{\rm B} \rangle$ but also the associated distribution $f(T_{\rm B})$. Such analysis is predicated on negligible interparticle interactions, 57,59,60,64 as supported by estimation of the interparticle interaction energies relative to $K_{\rm eff}V$, and by measurement of dilute NP dispersions. 44 The experimental $\langle T_{\rm B} \rangle$ vs $\langle D \rangle$ relationship from measurements of many NP

ensembles was then shown to be in quantitative, parameter-free agreement with eq 1 but only after accounting for (i) random shape anisotropy originating from the deviations from the spherical and (ii) an effective magnetic volume less than the nominal V due to a non-FM surface "dead" shell as deduced from suppressed $<\!D\!>$ -dependent high-field magnetization. This agreement was achieved with otherwise bulk-like Ni core properties, including saturation magnetization (M_s) and magnetocrystalline anisotropy. 44

While the above constitutes a significant advance, the quantitative agreement hinged on the assumption of an ~ 1 nm thick non-FM surface dead shell on the Ni NPs, as deduced indirectly from $<\!D\!>$ -dependent, low- $\!T\,M(H)$ data. 44 The true nature and origin of this dead shell and the resulting chemical and magnetic profiles within the Ni NPs remain unknown, which is the central issue we address here. Specifically, in this work, we employ both unpolarized and polarized small-angle neutron scattering (SANS) measurements and analyses to achieve sub-nanometer-resolution profiling of the chemical and magnetic average internal structures of these Ni NPs, resolving both the nature and origin of the non-FM dead shell.

After discussing experimental methods in the "Experimental Methods" section, the "Results and Discussion" section first reviews the $\langle D \rangle$ -dependent, low-TM(H) data that lead to the deduction of a nanometric non-FM dead shell on the surfaces of these Ni NPs. In our prior work, all such data were acquired at a single $T_s = 200$ °C. ⁴⁴ We then present T_s -dependent X-ray diffraction (XRD), transmission electron microscopy (TEM), and magnetometry data, revealing an unanticipated finding. Specifically, while all syntheses at $T_s \le 200$ °C result in similar XRD, TEM, and magnetometry, increasing T_s to just 250 °C completely extinguishes any signature of ferromagnetic FCC Ni, instead resulting in the non-FM nickel phosphide Ni₁₂P₅. The TOP used in this synthesis, and indeed many such colloidal NP syntheses, is the obvious source of the P required to form this phosphide, likely via diffusion-limited reactions promoted at higher T_s . Given this Ni₁₂P₅ formation at high T_s and the deduction of a non-FM shell at lower T_s , we thus form the hypothesis of a phosphide shell at all T_s , falling beneath the detection limits of standard XRD and TEM at low T_s . SANS techniques with varying levels of neutron spin polarization analysis are then applied to test this hypothesis directly. Unpolarized SANS data, which are dominated by structural rather than magnetic scattering, first reveal a chemically distinct nanometric shell on the Ni NPs with T_s-dependent shell thicknesses (as small as ~0.5 nm) in remarkable agreement with estimates of the non-FM shell thickness from magnetometry. This shell is further shown to have a nuclear scattering length density (SLD) consistent with Ni₁₂P₅. Fully polarized SANS, where the neutron spin is selected and analyzed both before and after scattering to enable isolation of purely magnetic scattering contributions, is then shown to be entirely consistent with the T_s-dependent core-shell model from unpolarized SANS with an FM Ni core with M_s very close to bulk Ni and negligible interparticle magnetic interactions. Finally, detailed T-dependent half-polarized SANS measurements, where the neutron spin is selected only prior to scattering, establish quantitative agreement between the extracted magnetic SLD and M(T) from magnetometry. An FM Ni core surrounded by a non-FM Ni₁₂P₅ shell is thus directly established, the core Ni having bulk-like M_s and Tdependence, with negligible interparticle magnetic interactions. These findings: (i) directly support prior assumptions used to

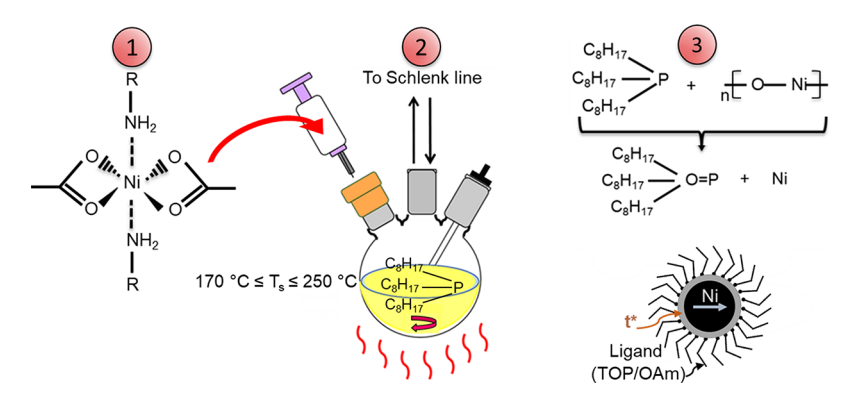


Figure 1. Synthesis scheme for Ni NPs: 1. Synthesis of a Ni-acetate-oleylamine (OAm) complex; 2. Hot injection into trioctylphosphine (TOP); 3. Reduction to Ni NPs coordinated by TOP and OAm ligands (thus forming trioctylphosphine oxide (TOPO)). Key variables in the synthesis are the TOP:OAm ratio, synthesis temperature (170 °C $\leq T_s \leq$ 250 °C), reaction time, and post-synthesis differential centrifugation conditions. The lower-right schematic illustrates resulting ferromagnetic Ni NPs, with dead-shell thickness t^* , and TOP and OAm ligands.

claim quantitative agreement with SP theory, 44 (ii) comprehensively elucidate the synthesis—structure—property relationships in these model Ni NP ensembles, (iii) are directly relevant to other colloidal synthesis involving TOP (and potentially other reducing agents), (iv) point to a potential route to facile ligand-free NP stabilization, and (v) further highlight the power of unpolarized/polarized SANS in magnetic NP science and technology.

■ EXPERIMENTAL METHODS

NP Synthesis. Ni NPs were synthesized *via* hot-injection methods as described in detail in prior work. He Briefly, the synthesis proceeds in three main steps as in Figure 1. Step 1 involves the formation of a Ni acetate—OAm complex by adding Ni acetonate tetrahydrate to OAm and then heating to 80 °C. In step 2, the Ni acetate—OAm solution (at 80 °C) is injected into hot TOP at $T_{\rm s}$ between 170 and 250 °C. The solution is then maintained at $T_{\rm s}$ (step 3) for reaction times between 30 min and 120 min, resulting in Ni NPs, dispersed in trioctylphosphine oxide (TOPO), OAm, and TOP. This entire process is performed under vacuum (~50 mTorr (6.66 Pa)). After synthesis, NP dispersions were flocculated, separated by centrifugation, and subject to further differential centrifugation for size selection.

As reported in detail earlier, ⁴⁴ Ni NPs synthesized by the above procedures had 4.7 nm \leq <D> \leq 22.3 nm (from TEM), controlled *via* the TOP/OAm ratio, $T_{s'}$ the reaction time, and post-synthesis differential centrifugation. The average relative dispersity (σ /<D>) was 0.20 over all studied NP ensembles, the best conditions producing σ /<D> \approx 0.1. ⁴⁴ Briefly, our prior characterization revealed FCC Ni with near-bulk lattice parameter and polycrystalline (or twinned) internal microstructure. ⁴⁴ Fourier transform infrared and Raman spectroscopies conclusively confirmed that both OAm and TOP serve as ligands, as shown in the schematic in Figure 1. ⁴⁴

Structural and Magnetic Characterization. In addition to the characterization just described, further TEM, XRD, and magnetometry were performed in the current work. For XRD, thick Ni NP films were drop-cast on Si/SiO_x substrates from a concentrated toluene dispersion. A Bruker D8-Discover diffractometer⁶⁵ with a Co K_{α} source and a 2D detector was then employed. For TEM, Ni NPs were drop-cast on carbon grids from dilute dispersions under slow evaporation, to promote monolayer formation. An FEI Tecnai T12 (120 kV)⁶⁵ was used for conventional bright-field imaging. Image analysis involved >1000 NPs in each ensemble, resulting in robust <*D*> and σ determinations. SQUID magnetometry was conducted in a Quantum Design Magnetic Property Measurement System,⁶⁵ from 2 to 300 K in μ_0H up to 6 T, on dry NP assemblies prepared by evaporation of dispersions in a gelatin capsule.

Small-Angle Neutron Scattering. SANS measurements on 50–120 mg dry NP ensembles were performed on the NG7 SANS

instrument at the NIST Center for Neutron Research. Unpolarized SANS data were obtained at scattering wave vector magnitudes (Q) of $0.0012\ to\ 0.16\ \mbox{\normalfont\AA}^{-1}$ using two sample-detector distances (2 and 15 m). Such measurements were performed at 300 K in $\mu_0 H = 7$ mT. As for all data in this work, H was applied along the x axis, perpendicular to the neutron beam (along z). Fully polarized SANS data (0.003 Å⁻¹ \leq $Q \le 0.12 \text{ Å}^{-1}$) were collected on the same instrument, with a double-V supermirror polarizer, an RF spin flipper, and a ³He spin analyzer. 66-69 Such measurements were made at 5 K after: (i) field cooling in $\mu_0 H_{FC}$ = +1.5 T then reversing the field to $H=-H_c$ (i.e., the negative coercive field, where the net M is zero) and (ii) field cooling in $\mu_0 H_{FC} = +1.5$ T and measuring in +1.5 T (i.e., close to saturation). These unpolarized and fully polarized SANS data were taken on NP ensembles synthesized at $T_s = 170$, 200, and 250 °C. For the $T_s = 170$ °C case, additional half-polarized SANS data (0.013 Å⁻¹ $\leq Q \leq 0.14 \text{ Å}^{-1}$) were also acquired by removing the ³He analyzer, *i.e.*, polarizing the incoming beam but with no polarization analysis of the scattered neutrons. Such measurements were performed after field-cooling in +1.5 T, reducing μ_0H to +7 mT, and then progressively warming and equilibrating in 25-30 K steps from 5 to 300 K. The specific procedures to reduce full two-dimensional (2D) $Q_x - Q_y$ "maps" to one-dimensional (1D) scattering cross section $(d\Sigma/d\Omega)$ vs Q profiles are different in each case (unpolarized, halfpolarized, and fully polarized) and are discussed in detail below. A full description of data reduction procedures can be found elsewhere. 66,67 Briefly, we used SANS polarization reduction software⁷⁰ and/or Igor Pro software 65,71 with unpolarized and polarized SANS macros to correct for any polarization inefficiency and/or ³He transmission time dependence and to reduce raw neutron detector data to 2D $Q_x - Q_y$ maps as well as 1D $(d\Sigma/d\Omega)$ vs Q profiles. Simulation and refinement (also discussed in detail below) were done with the SasView package, with the Q resolution function of the instrument accounted for via SasView's pinhole smearing algorithm.⁷²

RESULTS AND DISCUSSION

Basic Magnetometry Characterization. Reviewed first in Figure 2 are the <D>-dependent magnetometry data on $T_s = 200$ °C Ni NP ensembles that initially led to the hypothesis of a nanometric non-FM surface shell. As can be seen in Figure 2a, at this T_s , the M(H) at 2 K (which is below the < T_B > of all NP ensembles in this work) reveals the expected finite H_c and remanence (see ref 44 for a low H blow-up) but with two anomalous features. Specifically, M(H) contains a clear non-saturating component, while the high-H magnetization also lies significantly beneath the $T \rightarrow 0$ M_s of bulk Ni (58 emu/g (1 emu = 10^{-3} Am²) 46,47,73). Note that as described earlier, 44 a ligand mass correction was estimated and applied to these data (this is the origin of the magnetization error bars in Figure 2b),

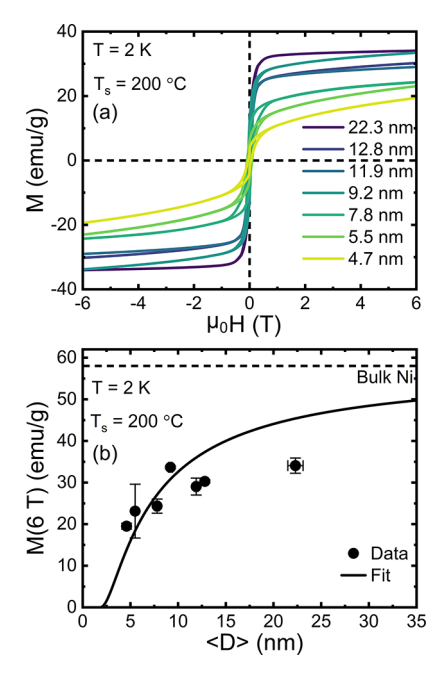


Figure 2. (a) Magnetization (M) vs applied magnetic field (μ_0H) at measurement temperature (T) of 2 K for dry Ni NP ensembles synthesized at temperature $T_s = 200$ °C. The average diameters (<D>) range from 4.7 to 22.3 nm (from transmission electron microscopy (TEM)), as shown. (b) 2 K high-field ($\mu_0H = 6.0$ T) M vs <D> (black points) extracted from (a). The solid black line is a fit to the core/shell model described in the text (see schematic in Figure 1), i.e., Ni cores with bulk saturation magnetization (M_s) surrounded by an M=0 shell of thickness $t^*=1.2$ nm. The solid horizontal line marks the T=0 M_s of bulk Ni. Error bars correspond to the standard error on <D> from fits to the size distribution and the standard error on M from the Ni NP mass (including the correction for ligand mass, which is discussed in detail in our prior work 44). Adapted with permission from ref 44. Copyright 2020 American Chemical Society. Note that $1 \text{ emu} = 10^{-3} \text{ Am}^2$.

but this is far too small to explain the suppression in M_s . The M_s suppression is highlighted in Figure 2b, which plots the high $\mu_0 H$ (6 T) 2 K magnetization vs $\langle D \rangle$, for comparison with the bulk Ni M_s (horizontal dashed line). Significantly, both the non-saturation in M(H) (Figure 2a) and the suppression of the high H magnetization (Figure 2b) become more prominent as <D> is decreased, consistent with a surface effect. The solid line in Figure 2b is in fact a fit to a simple model where an FM Ni core with bulk M_s is surrounded by a non-FM (M = 0) shell of thickness t^* (see the NP schematic in Figure 1), leading to high-field magnetization given by M_{HF} = $M_{s,\text{bulk}}[(\langle D \rangle - 2t^*)/\langle D \rangle]^3$, where $M_{s,\text{bulk}}$ is the bulk saturation magnetization. 44 As noted in our prior work, 44 the fit is reasonable, yielding $t^* = 1.2$ nm, i.e., an ~ 1 nm thick non-FM shell. It must be emphasized, however, that the M(< D>)data in Figure 2b could also be interpreted as evidencing a suppressed high-<D> M_s of \sim 35-40 emu/g. Moreover, as is clear from the magnetic NP literature, numerous other scenarios can result in reduced high-field magnetization in ferro- and ferrimagnetic NPs, including noncollinear/canted spin structures, 9,14,52,67,69,74 local antiferromagnetic regions, 61 etc. 61,62 Thus, while the assumption of a non-FM shell of 1.2 nm thickness (and a resulting FM volume less than the chemical volume) does result in quantitative agreement with eq 1 for the $\langle T_B \rangle$ vs $\langle D \rangle$ relation, 44 this deduction is nevertheless indirect and casts little light on the nature and origin of the dead shell.

 T_s -Dependent Characterization. The first insight into the nature and origin of the hypothesized non-FM dead shell on these Ni NPs comes from Figure 3, which presents XRD, TEM, and low-T (2 K) M(H) data as a function of the synthesis temperature T_s . As illustrated in Figure 3a,b, synthesis at $T_s \leq 200\,^{\circ}$ C results in simple XRD patterns consistent with FCC Ni, with near-bulk lattice parameters (3.526 and 3.529 Å in Figure 3a,b, respectively, compared to 3.524 Å in bulk⁷⁵). Consistent with this, standard-resolution bright-field TEM imaging (Figure 3d,e) indicates Ni NPs with structural parameters consistent with our prior work, 44 yielding

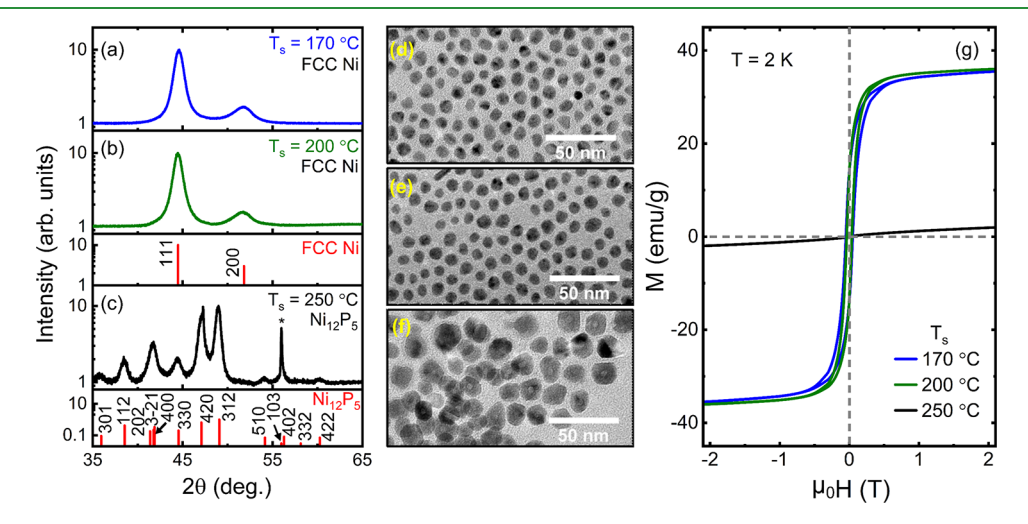


Figure 3. X-ray diffraction patterns from NP ensembles synthesized at temperatures (T_s) of (a) 170 °C, (b) 200 °C, and (c) 250 °C (solid blue, green, and black lines, respectively). <D>=8.3, 8.5, and 15.2 nm in (a), (b), and (c), respectively (from transmission electron microscopy (TEM)). The patterns in (a) and (b) index to face-centered-cubic (FCC) Ni, while (c) indexes to tetragonal Ni₁₂P₅ (see the red lines for standard patterns⁹¹). The unindexed peak marked with asterisks in (c) derives from Si powder used as a reference. (d–f) Conventional bright-field TEM images of NP ensembles synthesized at T_s = 170, 200, and 250 °C; scale bars are shown. (g) Magnetization (M) v_s applied magnetic field (μ_0H) at measurement temperature (T) of 2 K for the three NP ensembles in (a–f), i_s , i_s , i_s , i_s , and i_s , i_s ,

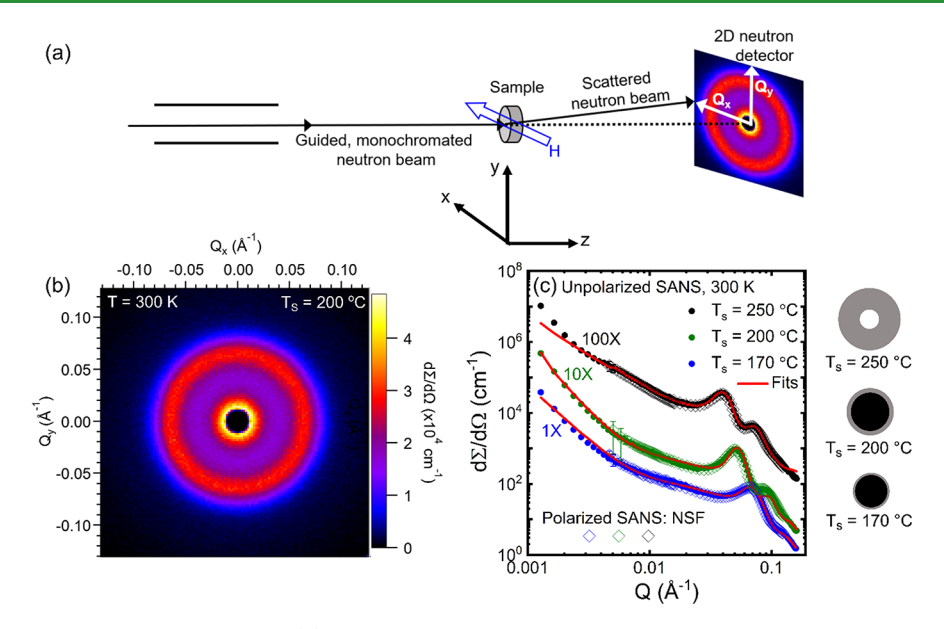


Figure 4. (a) Basic schematic for unpolarized SANS. (b) Example two-dimensional "map" of the unpolarized SANS cross section $(d\Sigma/d\Omega)$ vs Q_{xy} Q_{ν} , i.e., two orthogonal scattering wave vector components in the detector plane. The data shown were collected at measurement temperature T=300 K in applied magnetic field $\mu_0 H = 7.0$ mT, on a Ni NP ensemble synthesized at temperature $T_s = 200$ °C, with average diameter < D > = 11.5nm (from transmission electron microscopy (TEM)). (As for all data in this paper, H was applied along x, perpendicular to the neutron beam, which is parallel to z). Circular averaging of the type of isotropic data in (b) results in the $(d\Sigma/d\Omega)$ vs Q in (c), where Q is the wave vector magnitude. Blue, green, and black circles correspond to $T_s = 170$, 200, and 250 °C, respectively, with $\langle D \rangle = 8.3$, 11.5, and 15.2 nm (from TEM). The green and black curves have been displaced for clarity, i.e., multiplied by the shown factors of 10 and 100, respectively. Error bars correspond to one standard deviation and are typically smaller than the data points. Solid red lines are fits to the core—shell model discussed in the text. All fitting parameters are listed in Table 1. The extracted shell thickness (t^*) and total <D> are: t^* = 0.5 nm, <D> = 8.5 nm at 170 $^{\circ}$ C; t^* = 1.1 nm, <D> = 11.6 nm at 200 °C; and $t^* = 5.3$ nm, $\langle D \rangle = 15.5$ nm at 250 °C. The core and shell at 170 and 200 °C were fitted with the nuclear scattering length densities of Ni and Ni₁₂P₅, respectively; at 250 °C, the core was fitted with zero nuclear scattering length density, i.e., a hollow sphere. Note that the fits include a Qⁿ (generalized Porod) component clearly apparent at the lowest Q, which we ascribe to Porod scattering from naturally formed agglomerated long-range NP networks and/or excess ligands; the fitted n are listed in Table 1. As discussed in the text, the fits include both the Qresolution function of the instrument and particle size dispersity. The schematics to the right of (c) summarize the key fitting results, black corresponding to Ni, gray to Ni₁₂P₅, and white to vacuum. Also shown in (c) (larger open diamonds) are the full-polarization total non-spin-flip (NSF) SANS cross sections at 5 K measured at $H = -H_0$ i.e., the negative coercive field (zero net magnetization) after field cooling in +1.5 T (see Figure 5).

 $\langle D \rangle = 8.3$ and 8.5 nm and $\sigma / \langle D \rangle = 0.15$ and 0.13 for $T_s = 170$ and 200 °C, respectively. Consistent with these XRD and TEM data, the corresponding 2 K M(H) curves ($T_s = 170$ and 200 °C in Figure 3g) are in good agreement with Figure 2, indicating blocked FM behavior (see ref 44 for full Tdependent characterization, including the determination of $T_{\rm B}$ and its distribution) with suppressed high-H magnetization of ~35 emu/g. As shown in Figure 3c,f, this situation changes dramatically when T_s is increased by just 50 °C, to 250 °C. At this T_{s} , the XRD signature of FCC Ni is entirely extinguished and replaced with a distinctly more complex pattern. Comparison to potential phases leads to the conclusion that such patterns are closely consistent with the tetragonal Ni phosphide α -Ni₁₂P₅ (compare the data and reference pattern in Figure 3c), an equilibrium line compound in the Ni-P phase diagram (see Supporting Information Figure S1). Corresponding TEM images at $T_s = 250$ °C (Figure 3f) reveal a similarly striking change: A noticeable core-shell morphology emerges, potentially even suggesting a hollow core surrounded by a solid shell, as returned to below. Equally remarkable are the 2 K M(H) data for such $T_s = 250$ °C NPs (Figure 3g), which evidence no FM component at all, exhibiting only weak curvature and no measurable H_c or remanence. This is consistent with the reported magnetic properties of the Ni₁₂P₅ phase concluded from Figure 3c, which is thought to be paramagnetic, at least down to 5 K.76,77 Generally, ferromagnetism is quenched in Ni-P systems with P concentration above ~ 15 at $\%.^{78}$

The only obvious source of the P required to form the deduced Ni₁₂P₅ phase at $T_s = 250$ °C is the TOP used in this and many other colloidal NP syntheses. Scattered reports of phosphide formation in TOP-based Ni NP syntheses in fact exist, dating back at least as far as 2009. 79,80 Wang et al., for example, reported a crossover from Ni to Ni-P NPs with increasing T_s in TOP-based synthesis, including observation of Ni₁₂P₅.⁷⁹ Moreau et al. then found increasing P incorporation in Ni NPs at higher T_s, primarily via X-ray near-edge and extended absorption fine structure spectroscopies.81 Such effects were subsequently exploited for deliberate synthesis of Ni-P and Co-Ni-P phases using high-T_s TOP-based methods.^{82,83} The general picture that emerges is that in these synthesis routes, P from TOP can incorporate in Ni NPs, the extent of the P incorporation and the diffusion-limited reaction to phosphides being highly sensitive to T_s . Of particular relevance to the current work, Wang et al. also reported hollow-core Ni-P NPs at high T_s (as hinted at by Figure 3f), explained in terms of a Kirkendall effect due to inequivalent rates of in-diffusion of P and out-diffusion of Ni. 75 The prevalence of the specific Ni phosphide Ni₁₂P₅ also seems reasonable as this has been reported to lie close to the minimum in the "convex hull" of the Ni-P formation enthalpy vs P content curve.84

Table 1. Unpolarized SANS Fitting Parameters (from Figure 4c)^a

T_s (°C)	< <i>D</i> > (nm)	<i>t</i> * (nm)	S	f	n	$I_p \left(\mathrm{cm}^{-1} \ \mathrm{\AA}^{-n} \right)$	σ/ <d></d>
170	$8.5 \pm 0.08 (8.3)$	$0.5\pm0.02(0.6)$	0.30 ± 0.003	0.43 ± 0.001	3.0±0.016	$4.6 \times 10^{-5} \pm 1.4 \times 10^{-9}$	$0.38 \pm 0.004 (0.15)$
200	$11.6 \pm 0.05 (11.5)$	$1.1\pm0.02(1.2)$	0.15 ± 0.001	0.51 ± 0.001	3.4 ± 0.02	$2.7 \times 10^{-6} \pm 1.1 \times 10^{-9}$	$0.36 \pm 0.002(0.1)$
250	$15.5 \pm 0.02(15.2)$	$5.3\pm0.01(0.0)$	0.30 ± 0.001	0.49 ± 0.001	2.0 ± 0.01	0.034 ± 0.0002	$0.48 \pm 0.002 (0.28)$

"Shown in the table are the NP synthesis temperature (T_s) , total diameter (<D>), shell thickness (t^*) , scale factor (S), particle volume fraction (f), power-law (generalized Porod) exponent (n), power-law (generalized Porod) intensity or scale factor (I_p) , and log-normal dispersity $(\sigma/<D>)$ (note that the dispersity was applied only to the Ni core in the SasView fit). For t^* , the values in brackets are estimates from magnetometry for comparison. For <D> and $\sigma/<D>$, the values in brackets are from TEM, for comparison. For n and I_p , the defining equation is $I=I_p/Q^n$. Strictly, an additional fit parameter, $<D_{eff}>$, the approximate particle-to-particle spacing was also used in the hard-sphere structure factor. This is trivially related to <D> and the ligand thickness, however, and $<D_{eff}>$ was indeed found to be 1.1 nm to 1.6 nm larger than <D> in all cases, quite close to the expected ligand length. The parameter uncertainties shown were estimated from fitting and are dependent on the algorithm used (this was typically Levenberg–Marquardt, differential evolution, or Nelder–Mead simplex). Most algorithms use the covariance matrix at the optimum to estimate an uncertainty.

In light of the above literature and our observation of Ni₁₂P₅ NPs at $T_s = 250$ °C, a logical hypothesis based on Figures 2 and 3 is that P incorporation and shell formation also occur at T_s of 170 and 200 °C, simply to a much lesser extent, rendering them undetectable in basic XRD and TEM characterization. Specifically, a 1.2 nm thick non-FM Ni-P (likely $Ni_{12}P_5$) shell on Ni NPs synthesized at $T_s = 200$ °C would explain our magnetometry observations and could be difficult to detect in standard XRD and TEM. Further supporting this hypothesis, analysis of magnetometry data on $T_s = 170$ °C NPs using the aforementioned FM-core/non-FMshell model yields $t^* = 0.6$ nm, reduced from 1.2 nm at $T_s =$ 200 °C, consistent with the concept of diffusion-limited reaction to form a non-FM Ni-P shell. It must be noted, however, that while such observations are consistent with a Ni-P shell, direct verification is lacking.

Unpolarized SANS. Seeking a direct and quantitative test of the Ni-P shell hypothesis, a series of SANS measurements were performed on these NPs. SANS is ideally suited to this task as it is an ensemble-averaged technique that can provide detailed average chemical and magnetic internal structural information on NP ensembles, with sub-nm spatial resolution.^{66–69} To first probe the chemical structure primarily, unpolarized SANS data were acquired at 300 K using a set-up schematically depicted in Figure 4a. This was done on NP ensembles synthesized at T_s = 170, 200, and 250 °C, with respective $\langle D \rangle = 8.3$, 11.5, and 15.2 nm and $\sigma / \langle D \rangle = 0.15$, 0.10, and 0.28; all these values are from TEM. In the 170 and 250 °C cases, these are from the same sample batches as in Figure 3; in the 200 °C case, SANS was performed on a sample with (slightly) larger <D>. Shown first in Figure 4b is a representative 2D $Q_x - Q_y$ intensity map from the $T_s = 200$ °C sample. Such maps reveal highly isotropic scattering in the Q_x -Q, plane (as might be expected for random ensembles of nominally spherical NPs), and so reduction to 1D $d\Sigma/d\Omega$ vs Q profiles was done *via* circular averaging; $d\Sigma/d\Omega$ here is the absolute SANS cross section. This results in the data shown in Figure 4c, where $d\Sigma/d\Omega$ is plotted vs Q (on a \log_{10} - \log_{10} scale) for NP ensembles synthesized at 170, 200, and 250 °C (note that these curves are offset for clarity as described in the

The data in Figure 4c reveal a gradual fall off in $d\Sigma/d\Omega$ with Q, in addition to clear peaks and smaller shoulders around $\sim 0.05 \text{ Å}^{-1}$. That these peaks reflect the chemical structure of the NPs is confirmed by the solid red lines, which are SasView⁷² modeling results that closely reproduce the data. These fits correspond to locally close-packed NP ensembles modeled with a hard-sphere structure factor multiplied by a

core-shell NP form factor, the former generating the primary diffraction peak while the latter impacts the fine structure of the peak and shoulder. Explicitly, this modeling was achieved in SasView via the "add/multiply models" feature, combining a hard-sphere structure factor multiplied by a core-shell NP form factor (with NP diameter dispersity) and added to a generalized Porod component $(Q^{-n}, with n a constant$ exponent), the latter capturing scattering from agglomerated NPs and/or excess ligand, which is readily apparent at the lowest Q in Figure 4c. Significantly, such data cannot be fitted with a spherical form factor with any reasonable $\langle D \rangle$ and $\sigma /$ <D>, as documented in the Supporting Information (Figure S2). Based on our hypothesis from Figures 2 and 3, to fit the T_s = 170 $^{\circ}$ C and 200 $^{\circ}$ C data, the nuclear SLD of the NP core was fixed at that of pure Ni $(9.4 \times 10^{-6} \text{ Å}^{-2})$ and the chemical SLD of the NP shell was fixed at that of Ni₁₂P₅ (7.4 × 10⁻⁶ $Å^{-2}$). This leaves as primary fitting parameters the scale factor for the overall NP ensembles (S), the NP volume fraction (f), the total diameter ($\langle D \rangle$), the shell thickness (t^*), and the dispersity associated with the (log-normal) distribution of the diameter $(\sigma/\langle D \rangle)$. These parameters are tabulated in Table 1. The extracted $\langle D \rangle$ of 8.5 and 11.6 nm at $T_s = 170$ and 200 °C, respectively, are in excellent agreement with the 8.3 and 11.5 nm from TEM (also shown in Table 1). However, more importantly, the fitted t^* values for $T_s = 170$ and 200 °C NP ensembles are 0.5 and 1.1 nm, respectively, in remarkable agreement with the 0.6 and 1.2 nm estimated from magnetometry (Table 1). These unpolarized SANS data thus provide strong evidence not only of a chemically distinct shell with thickness in very close agreement with magnetometry estimates but also that this shell has nuclear SLD close to that of Ni₁₂P₅. The SANS sensitivity to the P content of the Ni-P shell is in fact good due to the quite different nuclear SLDs of Ni and P $(9.4 \times 10^{-6} \text{ and } 2.7 \times 10^{-6} \text{ Å}^{-2}, \text{ respectively})$, as detailed in the Supporting Information (Figure S1). The only non-ideality with the fits to the $T_s = 170$ and 200 °C data in Figure 4c is that σ /<D> values enlarged by a factor of \sim 2–3 relative to TEM were found (Table 1). These enlarged σ /<D> values were required to fit the intermediate Q region between \sim 0.004 and \sim 0.03 Å⁻¹, not only highlighting the much larger ensemble average for SANS compared to TEM but also likely pointing to some variance in the size of the locally closepacked clusters in these Ni NP ensembles, which we crudely account for here through increased $\sigma/\langle D \rangle$.

As is clear from close inspection of $d\Sigma/d\Omega$ vs Q in Figure 4c, the situation at $T_{\rm s}=250~^{\circ}{\rm C}$ is slightly different, specifically with respect to the positions, spacing, and intensities of the peak and shoulder. The same core–shell model can never-

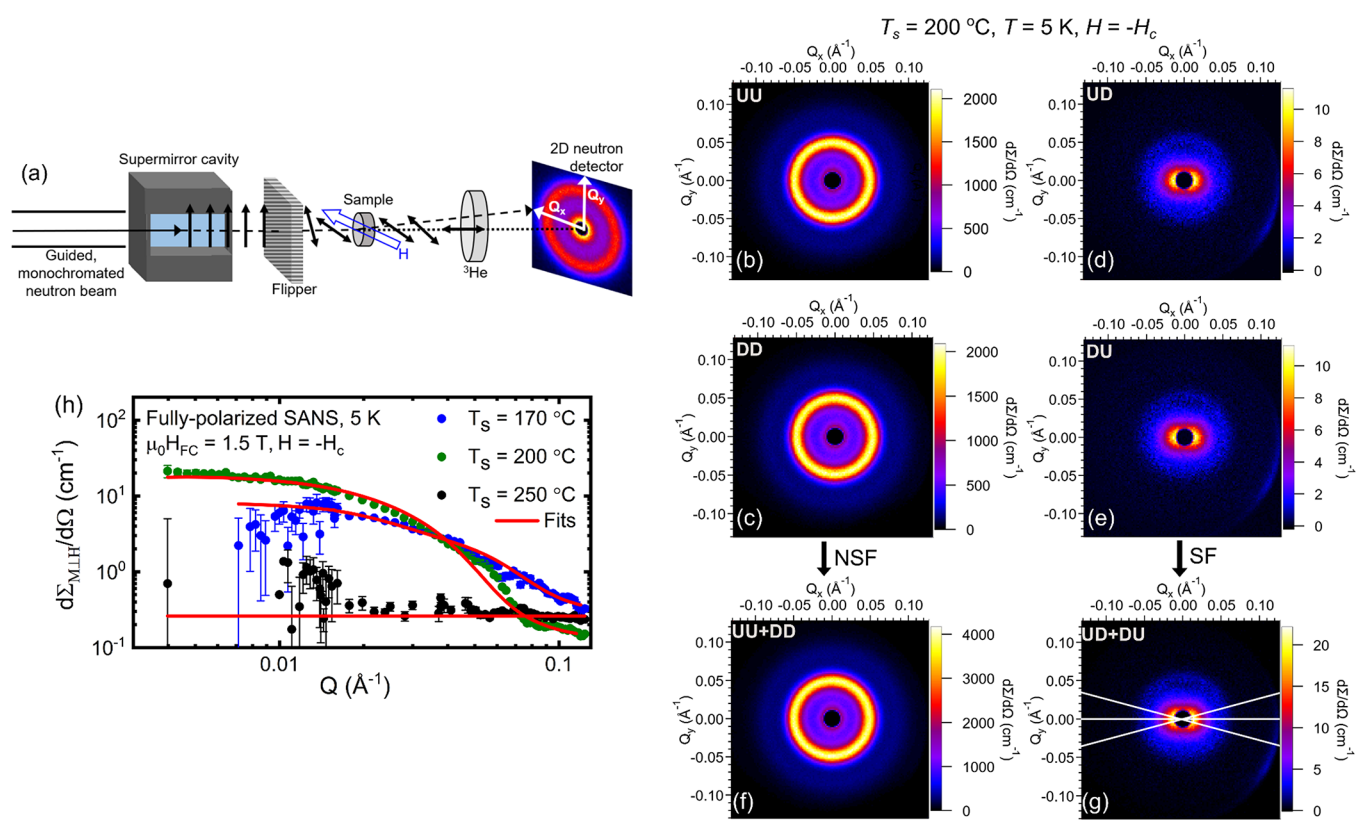


Figure 5. (a) Basic schematic for full-polarization SANS. (b-e) Two-dimensional "maps" of the SANS cross sections $vs\ Q_v\ Q_v\ i.e.$, two orthogonal scattering wave vector components in the detector plane. The up-up (UU), down-down (DD), up-down (UD), and down-up (DU) cross sections are shown in (b), (c), (d), and (e), respectively. Data were taken on the Ni NP ensemble synthesized at temperature $T_s = 200\ ^{\circ}\text{C}$ at a measurement temperature $T = 5\ \text{K}$ after field-cooling in $\mu_0 H_{FC} = +1.5\ \text{T}$ and reversing the applied field to $H = -H_{co}\ i.e.$, the negative coercive field (zero net magnetization). (As for all data in this paper, H was applied along x perpendicular to the neutron beam, which is parallel to z). (f) and (g) show the resulting total non-spin-flip (NSF) cross section (UU + DD) and total spin-flip (SF) cross section (UD + DU). Circular averaging of (f) produces the type of data shown as open diamonds in Figure 4c. Averaging the data in (g) within the illustrated $\pm 15^{\circ}$ sector produces the green points in (h), i.e., a purely magnetic cross section sensitive only to magnetization (M) perpendicular to H. We denote this $\left(\frac{d\Sigma_{\text{MLH}}}{d\Omega}\right)$, plotting it vs scattering wave vector magnitude Q in (h), for NP ensembles at $T_s = 170$, 200, and 250 °C (blue, green, and black, respectively). Error bars correspond to one standard deviation. Solid red lines are fits to the core—shell model discussed in the text with parameters in Table 1 (structural) and Table 2 (magnetic). All parameters were fixed at the values shown in Table 1 (from Figure 4c (unpolarized SANS)), except the core magnetic scattering length density (SLD), the particle volume fraction, and the polydispersity. The latter two parameters are discussed in the text. As also noted in the text, the scale factors used for the fits in (h) were fixed at two-thirds of those in Table 1 to obtain a magnetic SLD that properly accounts for all three magnetization components (in the x-, y-, and z-directions). As

theless describe these data but with very different nuclear SLD of the core, which in fact refined to zero, i.e., a vacuum core with a (hollow) Ni₁₂P₅ shell. While at first sight surprising, this is consistent with the suspicion from TEM (Figure 3f) and prior literature reports of hollow-shell Ni-P NPs at high T_e. ^{79,85} The fit in Figure 4c then yields $t^* = 5.3$ nm and $\langle D \rangle = 15.5$ nm (Table 1), the latter value again being in very good agreement with TEM (<D > = 15.2 nm). These unpolarized SANS results thus support a progression from a pure Ni core with a $Ni_{12}P_5$ shell at low T_s to a hollow core with a $Ni_{12}P_5$ shell at high T_s , the shell thickness increasing from 0.5 to 1.1 to 5.3 nm from 170 to 200 to 250 °C. This situation is summarized in the schematics to the right of Figure 4c, where the core and shell are drawn to scale. These conclusions are in good qualitative agreement with the notion of increasing extent of diffusion-limited reaction with TOP to form Ni-P at high T_s .

Full-Polarization SANS Measurements. Notably, the above-described fits in Figure 4c were obtained without accounting for the magnetic SLD of the Ni core. This is

because of the near-complete dominance of chemical scattering over magnetic scattering in unpolarized SANS from these NP ensembles as reinforced in Supporting Information Figure S3 and returned to below. Information on the magnetic structure of these NPs is nevertheless accessible via polarized SANS. Fully polarized SANS measurements were thus performed on the same NP ensembles using a set-up schematically depicted in Figure 5a. Briefly, control over the polarization of the incoming beam was achieved with a double-V supermirror polarizer in conjunction with an RF spin flipper, while polarization analysis of the scattered beam was achieved with a ³He analyzer. ^{66–69} In this manner, UU, DD, UD, and DU cross sections can be separately measured, i.e., "up-up", "downdown", "up-down", and "down-up" cross sections, where, e.g., "up-up" indicates "up" spin polarization of the incoming beam and "up" spin selection of the scattered beam 66-69 respect to the neutron polarization axis, parallel to H at the sample). References 66-69 provide full expressions for these various cross sections in their most general form. Below, we

provide the key expressions only for the specific analyses performed in this work (eqs 2-5) for simplicity.

 $Q_x - Q_y$ maps of the four polarized cross sections are shown in Figure 5b-e for the representative $T_s = 200$ °C case, although $T_s = 170$ °C and 250 °C ensembles were also measured. These measurements were made at 5 K after field cooling from 300 K in +1.5 T and then reversing the field to $-\mu_0 H_c$ (i.e., -27.5 mT for the data shown in Figure 5b-g). As returned below, this results in a situation where the net magnetization along H (parallel to the x axis) is close to zero, a situation that facilitates particularly insightful analysis. Specifically, at this point, there could be large net magnetization perpendicular to the field, large local dispersions in the magnetization vector, or any situation between. The UU and DD (i.e., non-spin-flip (NSF)) $Q_x - Q_y$ maps in Figure 5b,c reveal strong, highly isotropic scattering due to the dominance of chemical scattering contributions noted above. On the other hand, the UD and DU (i.e., spin-flip (SF)) cross sections (Figure 5d,e), which are equivalent in this scattering geometry in the absence of chiral spin structures, are purely magnetic in origin. Specifically, only the component of magnetization perpendicular to Q participates in magnetic scattering, such neutron selection rules holding for both polarized and unpolarized neutrons. For simplicity, we consider only sector cuts along the x and y axes (corresponding to Q_x and Q_y). In this case, any net magnetization component along the x axis (parallel to H) would give rise to a difference between UU and DD NSF cross sections in the sector cut along Q_{ν} as discussed elsewhere in this paper (see eqs 4 and 5). The SF scattering along Q_y is then proportional to the square of the magnetization component parallel to the z axis and perpendicular to H, whereas the SF scattering along Q_x is proportional to the sum of the squares of the perpendicular magnetization components along both y and z axes. The UD and DU maps in Figure 5d,e thus reveal not only much weaker scattering than the UU and DD (note the color scales) but also prominent anisotropy in the Q_x-Q_y plane. These maps are in fact "lobed" along the Q_x direction due to the neutron selection rules described above, as expected when the perpendicular components of the magnetization along y and z axes are equal. With isotropic distributions of the magnetizations along x, y, and z axes at H_c , one can write: 66,67

$$\rho_{\text{Mtotal}}^{2} = 1.5 \text{ C} \left[\left(\frac{d\Sigma}{d\Omega} \right)_{x}^{\text{UD}} + \left(\frac{d\Sigma}{d\Omega} \right)_{x}^{\text{DU}} \right]$$

$$= 3 \text{ C} \left[\left(\frac{d\Sigma}{d\Omega} \right)_{y}^{\text{UD}} + \left(\frac{d\Sigma}{d\Omega} \right)_{y}^{\text{DU}} \right]$$
(2)

Here, $\left(\frac{d\Sigma}{d\Omega}\right)_{x}^{\text{UD}}$, for example, is the UD cross section along the x direction, $ho_{ ext{Mtotal}}$ is the magnetic scattering length density (proportional to the total magnetization), and the pre-factors account for the fraction of magnetization that can be observed due to neutron scattering selection rules; C is a parameter that scales with the quantity of sample illuminated by the neutron beam. Based on eq 2 for $\rho_{ ext{Mtotal}}$, in Figure 5d,e, the SF scattering along Q_x should be twice that along Q_y (i.e., 3/1.5) since the magnetization parallel to Q_x is assumed to be equal to that along Q_y and Q_z at H_c . Reassuringly, the actual experimental value of this factor is 2.17 at $Q = 0.05 \text{ Å}^{-1}$, for example.

Following one common approach to further analysis of such fully polarized SANS data, $^{66-69}$ Figure 5f,g shows the total NSF and SF cross sections obtained by summing the UU and DD, and the UD and DU cross sections, respectively. Circular averaging of the NSF data in Figure 5f generates the open squares in Figure 4c, which almost exactly reproduce the unpolarized cross sections, as expected. This confirms the nearcomplete dominance of chemical contributions in the unpolarized cross section, consistent with the aforementioned lack of sensitivity to the magnetic SLD of the Ni core in these ensembles. (Note, however, that small differences between UU and DD cross sections can provide information about the magnetization parallel to H, as discussed in the next section).

Of higher interest is the summed SF cross section in Figure 5g, which we further analyze by taking $\pm 15^{\circ}$ sector cuts around the Q_x direction (as illustrated in the figure), thus generating the 1D $d\Sigma_{\rm MLH}/d\Omega$ vs Q profiles shown in Figure 5h for $T_{\rm s}$ = 170, 200, and 250 °C ensembles. Here,

$$d\Sigma_{\rm M\perp H}/d\Omega = C \left[\left(\frac{d\Sigma}{d\Omega} \right)_{x}^{\rm UD} + \left(\frac{d\Sigma}{d\Omega} \right)_{x}^{\rm DU} \right]$$
 (3)

is the magnetic scattering cross section due to magnetization components perpendicular to H (which is along the x axis) and C is the previously defined constant. Considering the $T_s = 170$ °C case first, $d\Sigma_{\rm MLH}/d\Omega$ in Figure 5h is seen to be essentially constant at low Q, rolling off in a fairly featureless fashion at higher Q, strongly reminiscent of a simple single-magnetic-NP form factor. Confirming this, the solid red line through the 170 °C data in Figure 5h is a SasView fit based on the previously determined $\langle D \rangle$ and t^* (from unpolarized SANS; Table 1), i.e., our Ni core/non-magnetic Ni₁₂P₅ shell model. Only the magnetic SLD of the Ni core, the magnetic SLD of the shell (which indeed consistently refined to zero), the NP volume fraction (f), and the dispersity (σ /<D>) were left as free parameters. The f and σ /<D> parameters refined to 0.14 and 0.32, respectively. While σ /<D> is practically the same as from fitting to unpolarized SANS data (Table 1), the f of 0.14 is smaller, leading to the important conclusion that the magnetic interparticle correlations are significantly weaker than the structural interparticle correlations. More importantly, the refined magnetic SLD of the Ni core is $1.31 \times 10^{-6} \text{ Å}^{-2}$, corresponding to 52 emu/g (1 emu = 10^{-3} Am^2), *i.e.*, within ~10% of the bulk low- $T M_s$ of Ni (Table 2). 46,47,73 In essence, this value sets the $Q \to 0$ value of $d\Sigma_{\rm M\perp H}/d\Omega$, the roll-off at higher Q being dictated by the FM Ni core form factor. Adding significantly to the conclusions from unpolarized SANS, this analysis thus confirms not only the core/shell structure but also the non-magnetic nature of the shell, the near-bulk M_s of the Ni core and the weak inter-particle magnetic correlations (at H_c), all of which were important in prior quantitative modeling of the SP < $T_B> vs <math><$ D> relation. ⁴⁴ As an aside, we note also that the solid line model fit in Figure 2b and this polarized SANS analysis result in near-identical M_s values, further confirming the validity of the ligand mass estimates used in our magnetometry analysis.

Moving to the $T_s = 200$ °C case in Figure 5h, the behavior is similar. The solid red line fit in this case is again to the coreshell model with previously determined structural parameters, the magnetic SLD of the Ni core this time refining to 1.47 \times 10^{-6} Å^{-2} , corresponding to 58 emu/g (Table 2), i.e., the exact low-T M_s of bulk Ni (f and $\sigma/<D> refined to 0.08 and 0.36,$ respectively). 46,47,73 This Ni core M_s was additionally

Table 2. Magnetic Parameters Extracted from 5 K Polarized SANS (from Figures 5h and 6d)^a

T₅ (°C)	magnetic SLD (10^{-6} Å^{-2}) from $\left(\frac{d\Sigma_{M\perp H}}{d\Omega}\right)$ $(H=-H_c)$	$M \text{ (emu/g)}$ from $\left(\frac{d\Sigma_{M\perp H}}{d\Omega}\right)$ $(H = -H_c)$	magnetic SLD (10^{-6} Å^{-2}) from $\left(\frac{d\Sigma_{\text{M}//\text{H}}}{d\Omega}\right) (\mu_0 H = 1.5 \text{ T})$	$M ext{ (emu/g)}$ from $\left(\frac{d\Sigma_{M//H}}{d\Omega}\right)$ $(\mu_0 H = 1.5$
170	1.31 ± 0.03	51.7 ± 1.0	1.27 ± 0.01	49.8 ± 0.4
200	1.47 ± 0.02	57.8 ± 0.7	1.40 ± 0.01	55.2 ± 0.4
250	0	0		

"Shown in the table are: The NP synthesis temperature (T_s) , the magnetic scattering length density (SLD) and magnetization (M) from the fits to $\left(\frac{d\Sigma_{\rm MLH}}{d\Omega}\right)$ at the coercive field (Figure 5h), and the magnetic SLD and M from the fits to $\left(\frac{d\Sigma_{\rm M/H}}{d\Omega}\right)$ at 1.5 T (Figure 6d). All values are for the Ni core. Data were not acquired in 1.5 T for the NP ensemble synthesized at $T_s = 250$ °C, hence the absence of table entries in that case. Note that 1 emu = 10^{-3} Am². The parameter uncertainties shown were estimated from fitting and are dependent on the algorithm used (this was typically Levenberg–Marquardt, differential evolution, or Nelder–Mead simplex). Most algorithms use the covariance matrix at the optimum to estimate an uncertainty. 92

corroborated in this case *via* complementary analysis (Supporting Information Figure S4) of the NSF cross section

(Figure 5f), yielding a comparable 55 emu/g and validating the assumption of isotropically distributed magnetization orientations at H_c . We note as an aside here that some minor structure around $\sim 0.07 \text{ Å}^{-1}$ in Figure 5h is not completely captured by this modeling, potentially pointing to some small level of interparticle magnetic correlations in this case. The overall situation then changes dramatically at $T_s = 250$ °C, where the $d\Sigma_{\rm MIH}/d\Omega$ cross section in Figure 5h essentially vanishes. (The small, essentially Q-independent background scattering can arise from several factors, including imperfect polarization correction, NSF contamination, incoherent scattering, etc.). A perfectly reasonable fit is obtained with zero magnetic SLD $(M_s = 0)$ in the core (Table 2), entirely consistent with the above deduction of a hollow core/non-FM shell structure. 79,83 Notably, the very different situation at $T_s = 250$ °C is only subtly apparent in unpolarized SANS (Figure 4c) but qualitatively obvious in polarized SANS (Figure 5h).

Complementary to the above, shown in Figure 6 are equivalent data for the $T_s = 200$ °C ensemble at the same measurement temperature of 5 K but in a large field $\mu_0H = +1.5$ T after field-cooling in the same. Panels (a) and (b) show DD and UU $Q_x - Q_y$ maps, respectively, in which the scattering is clearly lobed (in orthogonal directions in (a) and (b)), an indirect consequence of the large net magnetization along the field direction (x). Specifically, magnetic scattering appears only along the y-direction due to neutron selection rules but

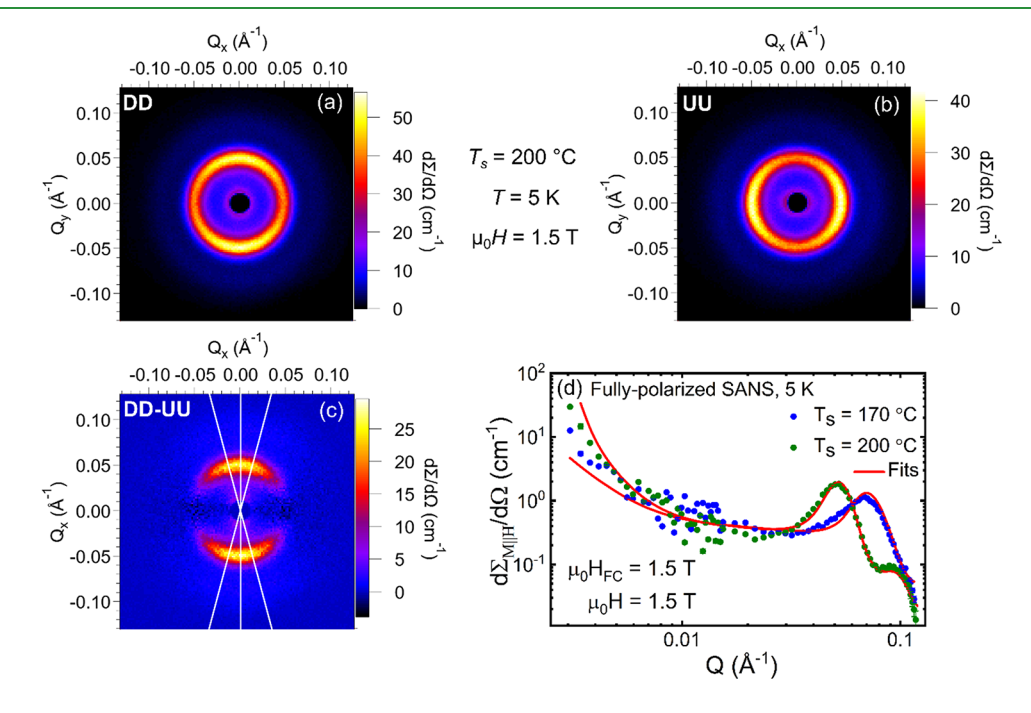


Figure 6. Full-polarization SANS data complementary to those in Figure 5b—h but acquired in large applied magnetic field (H), as opposed to the coercive field. The data are for the Ni NP ensemble synthesized at $T_s = 200\,^{\circ}\text{C}$, at a measurement temperature of 5 K in $\mu_0 H = +1.5$ T after field-cooling in $\mu_0 H_{FC} = +1.5$ T. (a) and (b) are two-dimensional "maps" of the SANS cross sections $vs\ Q_{xv}\ Q_y$ i.e., two orthogonal scattering wave vector components in the detector plane. The down—down (DD) and up—up (UU) cross sections are shown in (a) and (b), respectively. (c) then plots a squared, normalized DD-UU subtraction (see eq 4) along with the (vertical) $\pm 15^{\circ}$ sector cut used to generate a purely magnetic cross section sensitive only to the net magnetization (M) parallel to H, as discussed in the text. We denote this $\left(\frac{d\Sigma_{M//H}}{d\Omega}\right)$, plotting it vs scattering wave vector magnitude Q in (d), where equivalent data for the $T_s = 170\,^{\circ}\text{C}$ ensemble are also shown. Error bars correspond to one standard deviation and are smaller than the point size. The solid red lines here are fits to the same core—shell model as used in Figure 5, with all primary parameters fixed based on Figure 4c and Table 1, except the magnetic SLD. The deduced magnetic SLDs (also converted to magnetization) are shown in Table 2. As in Figure 4c, these fits include a Q^{*n} (generalized Porod) component; the scale of this contribution is significantly smaller than in Figure 4c as the ligands do not contribute to low-Q magnetic scattering. As discussed in the text, the fits include both the Q resolution function of the instrument and particle size dispersity.

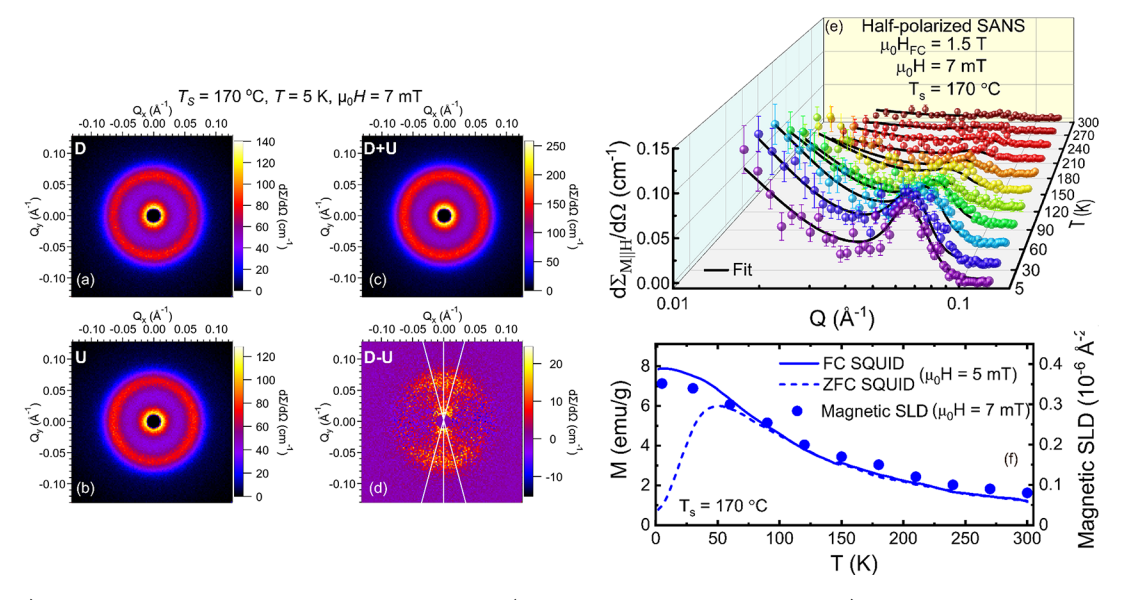


Figure 7. (a, b) Two-dimensional "maps" of the half-polarization (*i.e.*, incident beam polarization only) SANS cross sections $vs\ Q_{sp}$ *i.e.*, two orthogonal scattering wave vector components in the detector plane. (a) and (b) show the down (D) and up (U) cross sections for the NP ensemble synthesized at temperature $T_s = 170$ °C. Data were collected at measurement temperature T = 5 K after field-cooling in $\mu_0 H_{FC} = +1.5$ T and then reducing the field to $\mu_0 H = +7.0$ mT. (As for all data in this paper, H was applied along x, perpendicular to the neutron beam, which is parallel to z). (c) and (d) show the resulting D + U and D - U data. As discussed in the text, the shown (vertical) $\pm 15^{\circ}$ sector cut in (d) is used (see eq 5) to isolate a magnetic cross section sensitive only to magnetization (M) parallel to H. We denote this $\left(\frac{d\Sigma_{M//H}}{d\Omega}\right)$, plotting it vs scattering wave vector magnitude Q in (e), at T = 5, 30, 60, 90, 120, 150, 180, 210, 240, 270, and 300 K. Error bars correspond to one standard deviation. Solid black lines are the fits to the core—shell model described in the text. All parameters were fixed at values determined from Figure 4c (unpolarized SANS; Table 1) except the Ni core magnetic scattering length density (SLD). No Porod contribution was required here due to the larger minimum Q compared to Figures 4–6. As discussed in the text, the fits include both the Q resolution function of the instrument and particle size dispersity. The resulting Ni core magnetic SLD is shown $vs\ T$ in (f) (solid points), with equivalent M(T) (magnetization vs temperature) from SQUID magnetometry superimposed. M(T) was measured in 5.0 mT, zero-field-cooled (ZFC) and field-cooled (FC). Note that 1 emu = 10^{-3} Am².

adds to the structural scattering in the DD cross section and subtracts from it in the UU cross section. The DD–UU subtraction in (c) shows this lobing more clearly. This DD–UU cross section is not entirely magnetic in origin, however, and so, we followed a standard approach by taking a $\pm 15^{\circ}$ sector cut along the $Q_{\rm y}$ direction, as illustrated in Figure 6c. This extracts a nuclear-magnetic cross-term where the magnetic contribution is sensitive only to the net magnetization parallel to H. The purely magnetic cross section, $d\Sigma_{\rm M//H}/d\Omega_{\rm v}$, was then isolated using 66,67

$$\begin{split} d\Sigma_{\mathrm{M}\parallel\mathrm{H}}/d\Omega &= \rho_{\mathrm{M}\parallel\mathrm{H}}^{2} \\ &= 0.25 \ \mathrm{C} \Biggl(\left(\frac{d\Sigma}{d\Omega} \right)_{y}^{\mathrm{DD}} - \left(\frac{d\Sigma}{d\Omega} \right)_{y}^{\mathrm{UU}} \Biggr)^{2} \\ / \Biggl(\left(\frac{d\Sigma}{d\Omega} \right)_{x}^{\mathrm{DD}} + \left(\frac{d\Sigma}{d\Omega} \right)_{x}^{\mathrm{UU}} \Biggr) \end{split} \tag{4}$$

Similar to the notation used above, here $\left(\frac{d\Sigma}{d\Omega}\right)_{y}^{\text{UU}}$, for

example, is the UU cross section along the *y*-direction, $\rho_{\text{M}\parallel\text{H}}$ is the magnetic scattering length density (proportional to the net magnetization parallel to *H*), and *C* is the constant that scales with the quantity of sample illuminated by the neutron beam.

The resulting Q dependence of $d\Sigma_{\rm M//H}/d\Omega$ is shown in Figure 6d, not only for the $T_{\rm s}=200~^{\circ}{\rm C}$ ensemble highlighted in Figure 6a–c but also for $T_{\rm s}=170~^{\circ}{\rm C}$. In this high-field,

near-saturated condition, the form of the Q dependences of $d\Sigma_{\rm M//H}/d\Omega$ is very different to the $d\Sigma_{\rm M\perp H}/d\Omega$ curves in Figure 5h, instead having a peak/shoulder shape reminiscent of Figure 4c. This is because the large applied field mostly aligns the magnetization from one nanoparticle to the next, meaning that the extent of interparticle magnetization correlation becomes approximately equivalent to the interparticle structure correlation. The solid red line fits in this case are again to the core-shell model described above, this time with $S_1 < D > 1$ t^* , f, and $(\sigma/\langle D\rangle)$ (see Table 1) fixed based on the fits to Figure 4c and only the magnetic SLD of the shell and Ni core allowed to vary. The shell magnetic SLD tended to zero in both cases, and the core SLD refined to 1.27×10^{-6} and 1.40 \times 10⁻⁶ Å⁻² for the $T_s = 170$ and 200 °C cases, respectively, corresponding to 50 and 55 emu/g (Table 2). These values are again bulk-like, particularly for the 200 °C synthesized NP ensemble, potentially indicating slightly higher Ni structural quality at the elevated T_s (with larger t^* , however, as already noted).

Half-Polarization SANS Measurements. The above measurements and analyses conclusively support the picture of a Ni core with bulk-like FM properties surrounded by a non-FM $\mathrm{Ni_{12}P_5}$ shell at low T_s , evolving to a hollow core/non-FM $\mathrm{Ni_{12}P_5}$ shell at higher T_s . In the lower- T_s cases, low-T magnetometry and low-T polarized SANS are in near-exact quantitative agreement on the Ni core magnetization and the non-FM shell thickness, t^* . The magnetic aspects of these deductions derive only from 5 K data, however (Figures 5 and 6), leaving open the question of the T-dependence of the

magnetism. Probing this with fully polarized SANS measurements of the type shown in Figures 5 and 6 is prohibitively time consuming due to the substantial reduction in measured intensities. As a more viable alternative, we thus performed Tdependent half-polarized SANS measurements on the representative $T_s = 170$ °C NP ensemble. In this approach, the polarization of the incoming beam is maintained, but spin analysis of the scattered beam is not performed.66-69 Such measurements, which used only the 2 m (higher-Q) detector setting, were made after field cooling from 300 to 5 K in +1.5 T then reducing μ_0H to +7.0 mT, i.e., maintaining significant net magnetization parallel to H. D and U cross sections (see Figure 7a,b for an example at 5 K) were used to extract D + U and D - U intensities as shown in Figure 7c,d. As expected, the D + U Q_x – Q_y map reveals strong, isotropic scattering due to the dominance of chemical scattering contributions. As demonstrated in the Supporting Information (Figure S5), a circular average of the D + U data in Figure 7c almost exactly reproduces the unpolarized cross section in Figure 4c, as one would expect. The D - U scattering, on the other hand, although much weaker than D + U (see the color scales), is clearly lobed along Q_y, confirming significant net magnetization parallel to H. Along similar lines to the analyses above, the magnetic cross section $d\Sigma_{\mathrm{M//H}}/d\Omega$ was then extracted

$$\begin{split} d\Sigma_{\mathrm{M}\parallel\mathrm{H}}/d\Omega &= \rho_{\mathrm{M}\parallel\mathrm{H}}^2 \\ &= 0.25 \ C \Biggl(\Biggl(\frac{d\Sigma}{d\Omega} \Biggr)_y^\mathrm{D} - \left(\frac{d\Sigma}{d\Omega} \Biggr)_y^\mathrm{U} \Biggr)^2 \\ / \Biggl(\Biggl(\frac{d\Sigma}{d\Omega} \Biggr)_x^\mathrm{D} + \left(\frac{d\Sigma}{d\Omega} \Biggr)_x^\mathrm{U} \Biggr) \end{split} \tag{5}$$

where $\left(\frac{d\Sigma}{d\Omega}\right)_{y}^{U}$, for example, is the U cross section along the y direction. 66,67 This treatment is valid even without polarization analysis since any contribution to SF scattering from M perpendicular to H is effectively subtracted out in the

As shown in Figure 7e, $d\Sigma_{\rm M//H}/d\Omega$ and its Q dependence evolve significantly with increasing T, both the low Q tail and the $Q \approx 0.065 \text{ Å}^{-1}$ peak decreasing in intensity on warming. These two features arise from the decreasing amplitude of the inter-particle structure factor (modeled here with a hardsphere structure factor) convoluted with the FM form factor of the Ni core, meaning that a strong T dependence of this scattering cross section is to be expected in such SP Ni NP ensembles. At higher T, the low Q tail is, in fact, entirely suppressed, the only signature of magnetic scattering being a weak peak around 0.07 Å-1. The solid black line fits through these T-dependent data are again to our core-shell model, with all parameters fixed at previously determined values (Table 2) except the Ni core magnetic SLD. The very good fits in Figure 7e result in the T-dependent magnetic SLD values shown in Figure 7f, where the magnetic SLD on the right axis is converted to magnetization in emu/g on the left axis. The extracted net magnetization parallel to H from these halfpolarized SANS measurements is seen to decrease smoothly from \sim 7 emu/g at low T to around 1.5 emu/g at 300 K. Superimposed on these data in Figure 7f are SQUID magnetometry measurements of M(T) in a very similar

applied $\mu_0 H$ (5.0 mT) after both FC and ZFC. The agreement between the FC magnetizations from SQUID magnetometry and half-polarized SANS measurements (taken after FC) is remarkable not only in terms of the T dependence but also the absolute magnitudes. This observation extends the above conclusions by establishing not only a Ni core/Ni₁₂P₅ shell with bulk-like M_s in the Ni core but also T-dependent FM behavior in good accordance with magnetometry.

SUMMARY AND CONCLUSIONS

In summary, prior work establishing quantitative understanding of the superparamagnetic blocking temperature-size relationship in Ni nanoparticle ensembles was predicated on the indirect deduction of ferromagnetic volume less than the chemical volume due to surface dead shell formation. 44 Here, synthesis-temperature-dependent X-ray diffraction, transmission electron microscopy, and magnetometry measurements were first used to form the hypothesis of a chemical origin for this shell. This is based on surface Ni phosphide formation (specifically Ni₁₂P₅) due to diffusion-limited reaction with trioctylphosphine, a reducing agent, solvent, and ligand used in this and many other such colloidal nanoparticle syntheses. 1,2,79-83,87-90 A series of unpolarized, fully polarized, and half-polarized SANS measurements and analyses were then used to directly and completely probe the average internal chemical and magnetic structure of these NPs with sub-nm spatial resolution. The results not only confirm the formation of a nanometric Ni₁₂P₅ shell but additionally verify the bulklike magnitude and temperature dependence of the Ni core magnetization and, importantly, weak interparticle magnetic correlations (much weaker than the structural interparticle correlations), the other key assumptions in prior modeling of superparamagnetic behavior. 44 Detailed, quantitative insight into the synthesis temperature-dependent evolution from ferromagnetic Ni core/sub-nm non-ferromagnetic Ni₁₂P₅ shell to entirely non-ferromagnetic hollow $Ni_{12}P_5$ shells was

In addition to strong confirmation of key assumptions in prior parameter-free modeling of superparamagnetism and a detailed view of the synthesis-structure-property relations in these Ni nanoparticle ensembles, these findings point to some intriguing potential future directions. In particular, the deduced sub-nm control over the formation of Ni phosphide shells on these Ni nanoparticles suggests that it could be possible to develop this as a means to air-stabilize ferromagnetic metallic nanoparticles without organic ligands. Future work in this direction could assess the air stability of particles after organic ligand stripping as a function of the phosphide shell composition and thickness (controlled via the synthesis temperature) and potentially other synthesis variables. Statistical variations in shell thickness may well play a role in such issues, and it is noted that all parameters determined here from SANS are of course bulk ensemble averages. It would also be of interest to explore magnetically ordered Ni-P compositions (at lower P content), potentially generating a route to the one-step controlled synthesis of ferromagnetic core/magnetic phosphide shell nanoparticles. The work reported here provides a first step in these directions, supports prior assumptions in quantitative parameter-free modeling of superparamagnetism, and should serve to highlight both the P incorporation issue in this and related colloidal syntheses as well as the power of the currently available suite of SANS methods for such studies.

ASSOCIATED CONTENT

Supporting Information

The Supporting Information is available free of charge at https://pubs.acs.org/doi/10.1021/acsami.2c05558.

Ni-P equilibrium phase diagram with corresponding nuclear scattering length density data; additional information on core/shell modeling of SANS data; additional information on the lack of magnetic sensitivity in the unpolarized SANS data; additional full-polarization SANS data; and cross-checks of full-polarization and half-polarization SANS data (PDF)

AUTHOR INFORMATION

Corresponding Author

Chris Leighton – Department of Chemical Engineering and Materials Science, University of Minnesota, Minneapolis, Minnesota 55455, United States; orcid.org/0000-0003-2492-0816; Email: leighton@umn.edu

Authors

- Bhaskar Das Department of Chemical Engineering and Materials Science, University of Minnesota, Minneapolis, Minnesota 55455, United States
- Joseph T. Batley Department of Chemical Engineering and Materials Science, University of Minnesota, Minneapolis, Minnesota 55455, United States
- Kathryn L. Krycka NIST Center for Neutron Research, National Institute of Standards and Technology, Gaithersburg, Maryland 20899, United States; orcid.org/ 0000-0002-6393-3268
- Julie A. Borchers NIST Center for Neutron Research, National Institute of Standards and Technology, Gaithersburg, Maryland 20899, United States
- Patrick Quarterman NIST Center for Neutron Research, National Institute of Standards and Technology, Gaithersburg, Maryland 20899, United States
- Caroline Korostynski Department of Chemical Engineering and Materials Science, University of Minnesota, Minneapolis, Minnesota 55455, United States
- My Nguyen Department of Chemical Engineering and Materials Science, University of Minnesota, Minneapolis, Minnesota 55455, United States
- Ishita Kamboj Department of Chemical Engineering and Materials Science, University of Minnesota, Minneapolis, Minnesota 55455, United States
- Eray S. Aydil Department of Chemical and Biomolecular Engineering, New York University Tandon School of Engineering, Brooklyn, New York 11201, United States; orcid.org/0000-0002-8377-9480

Complete contact information is available at: https://pubs.acs.org/10.1021/acsami.2c05558

Author Contributions

C.L. and E.S.A. conceived of the study and oversaw its execution. J.T.B., B.D., C.K., M.N., and I.K. synthesized and characterized the nanoparticle assemblies under the guidance of E.S.A. and C.L. J.T.B., C.L., K.L.K., P.Q., and J.A.B. performed the SANS measurements. B.D., J.A.B., K.K., C.L., J.T.B., and P.Q. analyzed the SANS data. C.L., B.D., and J.A.B. wrote the paper with input from all authors.

Notes

The authors declare no competing financial interest.

ACKNOWLEDGMENTS

This work was supported primarily by the US Department of Energy through the University of Minnesota Center for Quantum Materials under DE-SC-0016371. Parts of this work were performed in the Characterization Facility, UMN, which receives partial support from NSF through the MRSEC program. Access to polarization capabilities on the NG7 SANS instrument was provided by the Center for High Resolution Neutron Scattering, a partnership between the National Institute of Standards and Technology and the National Science Foundation under agreement no. DMR-2010792. We are grateful to Jeff Krzywon for technical assistance on NG7 and to Shannon Watson and Taufique Hassan for assistance with the ³He polarization analyzer. Any mention of commercial products is for information only; it does not imply recommendation or endorsement by NIST.

REFERENCES

- (1) Hyeon, T. Chemical Synthesis of Magnetic Nanoparticles. *Chem. Commun.* **2003**, *3*, 927–934.
- (2) Nikam, A. V.; Prasad, B. L. V.; Kulkarni, A. A. Wet Chemical Synthesis of Metal Oxide Nanoparticles: A Review. *CrystEngComm* **2018**, *20*, 5091–5107.
- (3) Amiens, C.; Chaudret, B.; Ciuculescu-Pradines, D.; Collière, V.; Fajerwerg, K.; Fau, P.; Kahn, M.; Maisonnat, A.; Soulantica, K.; Philippot, K. Organometallic Approach for the Synthesis of Nanostructures. *New J. Chem.* **2013**, *37*, 3374–3401.
- (4) Sperling, R. A.; Parak, W. J. Surface Modification, Functionalization and Bioconjugation of Colloidal Inorganic Nanoparticles. *Philos. Trans. R. Soc., A* **2010**, *368*, 1333–1383.
- (5) Xia, Y.; Xiong, Y.; Lim, B.; Skrabalak, S. E. Shape-Controlled Synthesis of Metal Nanocrystals: Simple Chemistry Meets Complex Physics? *Angew. Chem., Int. Ed.* **2009**, *48*, 60–103.
- (6) Murray, C. B.; Sun, S.; Doyle, H.; Betley, T. Monodisperse 3d Transition-Metal (Co, Ni, Fe) Nanoparticles and Their Assembly into Nanoparticle Superlattices. MRS Bull. 2001, 26, 985–991.
- (7) Estrader, M.; López-Ortega, A.; Estradé, S.; Golosovsky, I. v.; Salazar-Alvarez, G.; Vasilakaki, M.; Trohidou, K. N.; Varela, M.; Stanley, D. C.; Sinko, M.; Pechan, M. J.; Keavney, D. J.; Peiró, F.; Suriñach, S.; Baró, M. D.; Nogués, J. Robust Antiferromagnetic Coupling in Hard-Soft Bi-Magnetic Core/Shell Nanoparticles. *Nat. Commun.* 2013, 4, 2960.
- (8) Zákutná, D.; Nižňanský, D.; Barnsley, L. C.; Babcock, E.; Salhi, Z.; Feoktystov, A.; Honecker, D.; Disch, S. Field Dependence of Magnetic Disorder in Nanoparticles. *Phys. Rev. X* **2020**, *10*, No. 031019.
- (9) Ijiri, Y.; Krycka, K. L.; Hunt-Isaak, I.; Pan, H.; Hsieh, J.; Borchers, J. A.; Rhyne, J. J.; Oberdick, S. D.; Abdelgawad, A.; Majetich, S. A. Correlated Spin Canting in Ordered Core-Shell Fe₃O₄/Mn_xFe_{3-x}O₄ Nanoparticle Assemblies. *Phys. Rev. B* **2019**, 99, No. 094421.
- (10) Sachan, M.; Bonnoit, C.; Majetich, S. A.; Ijiri, Y.; Mensah-Bonsu, P. O.; Borchers, J. A.; Rhyne, J. J. Field Evolution of Magnetic Correlation Lengths in ϵ -Co Nanoparticle Assemblies. *Appl. Phys. Lett.* **2008**, *92*, 152503.
- (11) Majetich, S. A.; Wen, T.; Booth, R. A. Functional Magnetic Nanoparticle Assemblies: Formation, Collective Behavior, and Future Directions. *ACS Nano* **2011**, *5*, 6081–6084.
- (12) Estrader, M.; López-Ortega, A.; Golosovsky, I. v.; Estradé, S.; Roca, A. G.; Salazar-Alvarez, G.; López-Conesa, L.; Tobia, D.; Winkler, E.; Ardisson, J. D.; Macedo, W. A. A.; Morphis, A.; Vasilakaki, M.; Trohidou, K. N.; Gukasov, A.; Mirebeau, I.; Makarova, O. L.; Zysler, R. D.; Peiró, F.; Dolors Baró, M.; Bergström, L.; Nogués, J. Origin of the Large Dispersion of Magnetic Properties in Nanostructured Oxides: Fe_xO/Fe₃O₄ Nanoparticles as a Case Study. *Nanoscale* **2015**, 3002–3015.

- (13) Evans, R. F. L.; Chantrell, R. W.; Chubykalo-Fesenko, O. Surface and Interface Effects in Magnetic Core-Shell Nanoparticles. MRS Bull. 2013, 38, 909-914.
- (14) Oberdick, S. D.; Abdelgawad, A.; Moya, C.; Mesbahi-Vasey, S.; Kepaptsoglou, D.; Lazarov, V. K.; Evans, R. F. L.; Meilak, D.; Skoropata, E.; van Lierop, J.; Hunt-Isaak, I.; Pan, H.; Ijiri, Y.; Krycka, K. L.; Borchers, J. A.; Majetich, S. A. Spin Canting across Core/Shell Fe₃O₄/Mn_xFe_{3-x}O₄ Nanoparticles. Sci. Rep. 2018, 8, 3425.
- (15) Lak, A.; Disch, S.; Bender, P. Embracing Defects and Disorder in Magnetic Nanoparticles. Adv. Sci. 2021, 8, 2002682.
- (16) Kodama, R. H. Magnetic Nanoparticles. J. Magn. Magn. Mater. 1999, 200, 359-372.
- (17) Majetich, S. A.; Jin, Y. Magnetization Directions of Individual Nanoparticles. Science 1999, 284, 470-473.
- (18) Leslie-Pelecky, D. L.; Rieke, R. D. Magnetic Properties of Nanostructured Materials. Chem. Mater. 1996, 8, 1770-1783.
- (19) Martín, J. I.; Nogués, J.; Liu, K.; Vicent, J. L.; Schuller, I. K. Ordered Magnetic Nanostructures: Fabrication and Properties. J. Magn. Magn. Mater. 2003, 256, 449-501.
- (20) Colombo, M.; Carregal-Romero, S.; Casula, M. F.; Gutiérrez, L.; Morales, M. P.; Böhm, I. B.; Heverhagen, J. T.; Prosperi, D.; Parak, W. J. Biological Applications of Magnetic Nanoparticles. Chem. Soc. Rev. 2012, 41, 4306-4334.
- (21) Manuchehrabadi, N.; Gao, Z.; Zhang, J.; Ring, H. L.; Shao, Q.; Liu, F.; McDermott, M.; Fok, A.; Rabin, Y.; Brockbank, K. G. M.; Garwood, M.; Haynes, C. L.; Bischof, J. C. Improved Tissue Cryopreservation Using Inductive Heating of Magnetic Nanoparticles. Sci. Transl. Med. 2017, 9, No. eaah4586.
- (22) Jeon, M.; Halbert, M. V.; Stephen, Z. R.; Zhang, M. Iron Oxide Nanoparticles as T1 Contrast Agents for Magnetic Resonance Imaging: Fundamentals, Challenges, Applications, and Prospectives. Adv. Mater. 2021, 33, 1906539.
- (23) Frey, N. A.; Peng, S.; Cheng, K.; Sun, S. Magnetic Nanoparticles: Synthesis, Functionalization, and Applications in Bioimaging and Magnetic Energy Storage. Chem. Soc. Rev. 2009, 38,
- (24) Das, R.; Alonso, J.; Nemati Porshokouh, Z.; Kalappattil, V.; Torres, D.; Phan, M.-H.; Garaio, E.; Ángel García, J.; Luis Sanchez Llamazares, J.; Srikanth, H. Tunable High Aspect Ratio Iron Oxide Nanorods for Enhanced Hyperthermia. J. Phys. Chem. C 2016, 120, 10086-10093.
- (25) Wang, J. P. FePt Magnetic Nanoparticles and Their Assembly for Future Magnetic Media. Proc. IEEE 2008, 96, 1847-1863.
- (26) Mohtasebzadeh, A. R.; Ye, L.; Crawford, T. M. Magnetic Nanoparticle Arrays Self-Assembled on Perpendicular Magnetic Recording Media. Int. I. Mol. Sci. 2015, 16, 19769.
- (27) Terris, B. D.; Thomson, T. Nanofabricated and Self-Assembled Magnetic Structures as Data Storage Media. J. Phys. D: Appl. Phys. 2005, 38, R199.
- (28) Grü, T. A.; Lassenberger, A.; van Oostrum, P. D. J.; Rennhofer, H.; Zirbs, R.; Capone, B.; Vonderhaid, I.; Amenitsch, H.; Lichtenegger, H. C.; Reimhult, E. Core-Shell Structure of Monodisperse Poly(Ethylene Glycol)-Grafted Iron Oxide Nanoparticles Studied by Small-Angle X-Ray Scattering. Chem. Mater. **2015**, 27, 4763-4771.
- (29) Xu, X.; Wang, W.; Zhou, W.; Shao, Z. Recent Advances in Novel Nanostructuring Methods of Perovskite Electrocatalysts for Energy-Related Applications. Small Methods 2018, 2, 1800071.
- (30) Kačenka, M.; Kaman, O.; Jirák, Z.; Maryško, M.; Zvátora, P.; Vratislav, S.; Lukeš, I. Magnetic Properties of La_{1-x}Sr_xMnO₃ Nanoparticles Prepared in a Molten Salt. J. Appl. Phys. 2014, 115, 17B525.
- (31) Thorat, N. D.; Shinde, K. P.; Pawar, S. H.; Barick, K. C.; Betty, C. A.; Ningthoujam, R. S. Polyvinyl Alcohol: An Efficient Fuel for Synthesis of Superparamagnetic LSMO Nanoparticles for Biomedical Application. Dalton Trans. 2012, 41, 3060-3071.
- (32) Yu, H. C.; Fung, K. Z.; Guo, T. C.; Chang, W. L. Syntheses of Perovskite Oxides Nanoparticles $La_{1-x}Sr_xMO_{3-\delta}$ (M = Co and Cu) as

- Anode Electrocatalyst for Direct Methanol Fuel Cell. Electrochim. Acta 2004, 50, 811-816.
- (33) Ma, M.; Chen, Y.; Tong, Z.; Liu, Y.; Ma, Y.; Wang, R.; Bi, Y.; Liao, Z. Research Progress of Magnetic Bismuth-Based Materials in Photocatalysis: A Review. J. Alloys Compd. 2021, 886, No. 161096.
- (34) Prakash, M.; Kavitha, H. P.; Abinaya, S.; Vennila, J. P.; Lohita, D. Green Synthesis of Bismuth Based Nanoparticles and Its Applications - A Review. Sustainable Chem. Pharm. 2022, 25, No. 100547.
- (35) Wang, X.; Zhang, Y.; Wu, Z. Magnetic and Optical Properties of Multiferroic Bismuth Ferrite Nanoparticles by Tartaric Acid-Assisted Sol-Gel Strategy. Mater. Lett. 2010, 64, 486-488.
- (36) Kandasamy, G. Recent Advancements in Manganite Perovskites and Spinel Ferrite-Based Magnetic Nanoparticles for Biomedical Theranostic Applications. Nanotechnology 2019, 30, 502001.
- (37) Jiang, Y.; Bridges, F.; Sundaram, N.; Belanger, D. P.; Anderson, I. E.; Mitchell, J. F.; Zheng, H. Study of the Local Distortions of the Perovskite System La_{1-x}Sr_xCoO₃ (0≤x≤0.35) Using the Extended X-Ray Absorption Fine Structure Technique. Phys. Rev. B 2009, 80, No. 144423.
- (38) Christodoulides, J. A.; Zhang, Y.; Hadjipanayis, G. C.; Fountzoulas, C. CoPt and FePt Nanoparticles for High Density Recording Media. IEEE Trans. Magn. 2000, 36, 2333-2335.
- (39) Sellmyer, D. J.; Balamurugan, B.; Das, B.; Mukherjee, P.; Skomski, R.; Hadjipanayis, G. C. Novel Structures and Physics of Nanomagnets (Invited). J. Appl. Phys. 2015, 117, 172609.
- (40) Yu, Y.; Mukherjee, P.; Tian, Y.; Li, X. Z.; Shield, J. E.; Sellmyer, D. J. Direct Chemical Synthesis of L10 -FePtAu Nanoparticles with High Coercivity. Nanoscale 2014, 6, 12050-12055.
- (41) Sellmyer, D. J.; Yan, M.; Xu, Y.; Skomski, R. High-Anisotropy Nanocluster Films for High-Density Perpendicular Recording. IEEE Trans. Magn. 2005, 41, 560-565.
- (42) Ebbing, A.; Hellwig, O.; Agudo, L.; Eggeler, G.; Petracic, O. Tuning the Magnetic Properties of Co Nanoparticles by Pt Capping. Phys. Rev. B 2011, 84, No. 012405.
- (43) Zhou, G.; Wang, Y. Q.; Byun, J. H.; Yi, J. W.; Yoon, S. S.; Cha, H. J.; Lee, J. U.; Oh, Y.; Jung, B. M.; Moon, H. J.; Chou, T. W. High-Strength Single-Walled Carbon Nanotube/Permalloy Nanoparticle/ Poly(Vinyl Alcohol) Multifunctional Nanocomposite Fiber. ACS Nano 2015, 9, 11414-11421.
- (44) Batley, J. T.; Nguyen, M.; Kamboj, I.; Korostynski, C.; Aydil, E. S.; Leighton, C. Quantitative Understanding of Superparamagnetic Blocking in Thoroughly Characterized Ni Nanoparticle Assemblies. Chem. Mater. 2020, 32, 6494-6506.
- (45) Batlle, X.; Labarta, A. Finite-Size Effects in Fine Particles: Magnetic and Transport Properties. J. Phys. D: Appl. Phys. 2002, 35,
- (46) O'Handley, R. C. Modern Magnetic Materials: Principles and Applications; John Wiley: New York; USA, 2000.
- (47) Coey, J. M. D. Magnetism and Magnetic Materials; Cambridge University Press: Cambridge; UK, 2010.
- (48) Bedanta, S.; Kleemann, W. Supermagnetism. J. Phys. D: Appl. Phys. 2009, 42, No. 013001.
- (49) Brown, W. F. Thermal Fluctuations of a Single-Domain Particle. Phys. Rev. 1963, 130, 1677.
- (50) Néel, L. Théorie Du Trainage Magnétique Des Ferromagnétiques En Grains Fins Avec Application Aux Terres Cuites. Ann. Géophysique 1949, 5, 99-136.
- (51) Bean, C. P.; Livingston, J. D. Superparamagnetism. J. Appl. Phys. 2009, 30, S120.
- (52) Baaziz, W.; Pichon, B. P.; Fleutot, S.; Liu, Y.; Lefevre, C.; Greneche, J. M.; Toumi, M.; Mhiri, T.; Begin-Colin, S. Magnetic Iron Oxide Nanoparticles: Reproducible Tuning of the Size and Nanosized-Dependent Composition, Defects, and Spin Canting. J. Phys. Chem. C 2014, 118, 3795-3810.
- (53) Dutta, P.; Pal, S.; Seehra, M. S.; Shah, N.; Huffman, G. P. Size Dependence of Magnetic Parameters and Surface Disorder in Magnetite Nanoparticles. J. Appl. Phys. 2009, 105, No. 07B501.

- (54) Pan, Y.; Jia, R.; Zhao, J.; Liang, J.; Liu, Y.; Liu, C. Size-Controlled Synthesis of Monodisperse Nickel Nanoparticles and Investigation of Their Magnetic and Catalytic Properties. *Appl. Surf. Sci.* **2014**, *316*, 276–285.
- (55) Fonseca, F. C.; Goya, G. F.; Jardim, R. F.; Muccillo, R.; Carreño, N. L. V.; Longo, E.; Leite, E. R. Superparamagnetism and Magnetic Properties of Ni Nanoparticles Embedded in SiO₂. *Phys. Rev. B* **2002**, *66*, No. 104406.
- (56) Park, J.; An, K.; Hwang, Y.; Park, J. E. G.; Noh, H. J.; Kim, J. Y.; Park, J. H.; Hwang, N. M.; Hyeon, T. Ultra-Large-Scale Syntheses of Monodisperse Nanocrystals. *Nat. Mater.* **2004**, *3*, 891–895.
- (57) Bruvera, I. J.; Mendoza Zélis, P.; Pilar Calatayud, M.; Goya, G. F.; Sánchez, F. H. Determination of the Blocking Temperature of Magnetic Nanoparticles: The Good, the Bad, and the Ugly. *J. Appl. Phys.* **2015**, *118*, 184304.
- (58) Denardin, J. C.; Brandl, A. L.; Knobel, M.; Panissod, P.; Pakhomov, A. B.; Liu, H.; Zhang, X. X. Thermoremanence and Zero-Field-Cooled/Field-Cooled Magnetization Study of $\text{Co}_x(\text{SiO}_2)_{1-x}$ Granular Films. *Phys. Rev. B* **2002**, *65*, No. 064422.
- (59) Micha, J. S.; Dieny, B.; Régnard, J. R.; Jacquot, J. F.; Sort, J. Estimation of the Co Nanoparticles Size by Magnetic Measurements in Co/SiO₂ Discontinuous Multilayers. *J. Magn. Magn. Mater.* **2004**, 272–276, E967–E968.
- (60) Mamiya, H.; Ohnuma, M.; Nakatani, I.; Furubayashim, T. Extraction of Blocking Temperature Distribution from Zero-Field-Cooled and Field-Cooled Magnetization Curves. *IEEE Trans. Magn.* **2005**, *41*, 3394–3396.
- (61) Kleibert, A.; Balan, A.; Yanes, R.; Derlet, P. M.; Vaz, C. A. F.; Timm, M.; Fraile Rodríguez, A.; Béché, A.; Verbeeck, J.; Dhaka, R. S.; Radovic, M.; Nowak, U.; Nolting, F. Direct Observation of Enhanced Magnetism in Individual Size- and Shape-Selected 3d Transition Metal Nanoparticles. *Phys. Rev. B* **2017**, *95*, No. 195404.
- (62) Balan, A.; Derlet, P. M.; Rodríguez, A. F.; Bansmann, J.; Yanes, R.; Nowak, U.; Kleibert, A.; Nolting, F. Direct Observation of Magnetic Metastability in Individual Iron Nanoparticles. *Phys. Rev. Lett.* **2014**, *112*, No. 107201.
- (63) Oyarzún, S.; Tamion, A.; Tournus, F.; Dupuis, V.; Hillenkamp, M. Size Effects in the Magnetic Anisotropy of Embedded Cobalt Nanoparticles: From Shape to Surface. *Sci. Rep.* **2015**, *5*, 14749.
- (64) de Julián Fernández, C. Influence of the Temperature Dependence of Anisotropy on the Magnetic Behavior of Nanoparticles. *Phys. Rev. B* **2005**, 72, No. 054438.
- (65) Any mention of commercial products is for information only; it does not imply recommendation or endorsement by NIST.
- (66) Krycka, K.; Chen, W.; Borchers, J.; Maranville, B.; Watson, S. Polarization-Analyzed Small-Angle Neutron Scattering. I. Polarized Data Reduction Using Pol-Corr. *J. Appl. Crystallogr.* **2012**, *45*, 546–553.
- (67) Krycka, K.; Borchers, J.; Ijiri, Y.; Booth, R.; Majetich, S. Polarization-Analyzed Small-Angle Neutron Scattering. II. Mathematical Angular Analysis. *J. Appl. Crystallogr.* **2012**, *45*, 554–565.
- (68) Michels, A. Magnetic Small-Angle Neutron Scattering of Bulk Ferromagnets. J. Phys.: Condens. Matter 2014, 26, No. 383201.
- (69) Mühlbauer, S.; Honecker, D.; Périgo, É. A.; Bergner, F.; Disch, S.; Heinemann, A.; Erokhin, S.; Berkov, D.; Leighton, C.; Eskildsen, M. R.; Michels, A. Magnetic Small-Angle Neutron Scattering. *Rev. Mod. Phys.* **2019**, *91*, No. 015004.
- (70) https://github.com/krycket. (Accessed 03/30/2022).
- (71) https://github.com/sansigormacros. (Accessed 03/30/2022).
- (72) SasView Small Angle Scattering Analysis https://www.sasview.org/. (Accessed 03/30/2022).
- (73) Crangle, J.; Goodman, G. M. The Magnetization of Pure Iron and Nickel. *Proc. R. Soc. A* **1971**, 321, 477–491.
- (74) Krycka, K. L.; Booth, R. A.; Hogg, C. R.; Ijiri, Y.; Borchers, J. A.; Chen, W. C.; Watson, S. M.; Laver, M.; Gentile, T. R.; Dedon, L. R.; Harris, S.; Rhyne, J. J.; Majetich, S. A. Core-Shell Magnetic Morphology of Structurally Uniform Magnetite Nanoparticles. *Phys. Rev. Lett.* **2010**, *104*, No. 207203.

- (75) Taylor, A. Lattice Parameters of Binary Nickel Cobalt Alloys. J. Inst. Met. 1950, 77, 585–594.
- (76) Ping, H. M.; Chen, Y. Z.; Zeng, D. Q.; Xu, R.; Guo, H. Z.; Wang, L. S.; Peng, D. L. Preparation of Gold-Nickel Phosphide Core-Shell Nanoparticles via a Facile Solution Method. *Appl. Mech. Mater.* **2014**, *464*, 64–68.
- (77) Costa, D. C.; Soldati, A. L.; Pecchi, G.; Bengoa, J. F.; Marchetti, S. G.; Vetere, V. Preparation and Characterization of a Supported System of Ni₂P/Ni₁₂P₅ Nanoparticles and Their Use as the Active Phase in Chemoselective Hydrogenation of Acetophenone. *Nanotechnology* **2018**, *29*, 215702.
- (78) Szpunar, B.; Aus, M.; Cheung, C.; Erb, U.; Palumbo, G.; Szpunar, J. A. Magnetism in Nanostructured Ni–P and Co–W Alloys. *J. Magn. Mater.* **1998**, *187*, 325–336.
- (79) Wang, J.; Johnston-Peck, A. C.; Tracy, J. B. Nickel Phosphide Nanoparticles with Hollow, Solid, and Amorphous Structures. *Chem. Mater.* **2009**, 21, 4462–4467.
- (80) Sasaki, S.; Kurish, J.; Robbennolt, S.; Yan, Y.; Garcia, E.; Tolbert, S. H. Covalent Bonding-Based Adhesion Method for Rigidly Coupling Metal Nanocrystals to Metal and Metal Oxide Surfaces. *ACS Appl. Nano Mater.* **2021**, *4*, 3426–3433.
- (81) Moreau, L. M.; Ha, D. H.; Bealing, C. R.; Zhang, H.; Hennig, R. G.; Robinson, R. D. Unintended Phosphorus Doping of Nickel Nanoparticles during Synthesis with TOP: A Discovery through Structural Analysis. *Nano Lett.* **2012**, *12*, 4530–4539.
- (82) Marusak, K. E.; Johnston-Peck, A. C.; Wu, W. C.; Anderson, B. D.; Tracy, J. B. Size and Composition Control of CoNi Nanoparticles and Their Conversion into Phosphides. *Chem. Mater.* **2017**, *29*, 2739–2747.
- (83) Sarac, M. F.; Wu, W. C.; Tracy, J. B. Control of Branching in Ni_3C_{1-x} Nanoparticles and Their Conversion into $Ni_{12}P_5$ Nanoparticles. *Chem. Mater.* **2014**, *26*, 3057–3064.
- (84) Delsante, S.; Schmetterer, C.; Ipser, H.; Borzone, G. Thermodynamic Investigation of the Ni-Rich Side of the Ni-P System. *J. Chem. Eng. Data* **2010**, *55*, 3468–3473.
- (85) Moreau, L. M.; Ha, D. H.; Zhang, H.; Hovden, R.; Muller, D. A.; Robinson, R. D. Defining Crystalline/Amorphous Phases of Nanoparticles through X-Ray Absorption Spectroscopy and X-Ray Diffraction: The Case of Nickel Phosphide. *Chem. Mater.* **2013**, *25*, 2394–2403.
- (86) $Q_x Q_y$ maps of the UD and DU spin-flip cross sections (not shown in Fig. 6) showed no significant $d\Sigma_{\rm MLH}/d\Omega$ scattering along the x and y directions in this near-saturated magnetic state, as expected. Notably, however, the intensity in those maps is maximum along the diagonals (i.e., $\pm 45^\circ$ from the x and y axes), also consistent with high M parallel to H.
- (87) Bi, Y.; Yuan, Y.; Exstrom, C. L.; Darveau, S. A.; Huang, J. Air Stable, Photosensitive, Phase Pure Iron Pyrite Nanocrystal Thin Films for Photovoltaic Application. *Nano Lett.* **2011**, *11*, 4953–4957.
- (88) Yang, Z.; Klabunde, K. J. Synthesis of Nearly Monodisperse Palladium (Pd) Nanoparticles by Using Oleylamine and Trioctylphosphine Mixed Ligands. *J. Organomet. Chem.* **2009**, 694, 1016–1021.
- (89) Muthuswamy, E.; Kharel, P. R.; Lawes, G.; Brock, S. L. Control of Phase in Phosphide Nanoparticles Produced by Metal Nanoparticle Transformation: Fe_2P and FeP. ACS Nano 2009, 3, 2383–2393.
- (90) Cingarapu, S.; Yang, Z.; Sorensen, C. M.; Klabunde, K. J. Synthesis of Indium Nanoparticles: Digestive Ripening under Mild Conditions. *Inorg. Chem.* **2011**, *50*, 5000–5005.
- (91) Crystallography Open Database: COD#1537573.
- (92) https://www.sasview.org/docs/user/qtgui/Perspectives/Fitting/optimizer.html. (Accessed 03/30/2022).